University of Groningen

Aneuploidy renders cancer cells vulnerable to mitotic checkpoint inhibition

Cohen-Sharir, Yael; McFarland, James M; Abdusamad, Mai; Marquis, Carolyn; Bernhard, Sara V; Kazachkova, Mariya; Tang, Helen; Ippolito, Marica R; Laue, Kathrin; Zerbib, Johanna

IMPORTANT NOTE: You are advised to consult the publisher's version (publisher's PDF) if you wish to cite from it. Please check the document version below.

Document Version
Publisher's PDF, also known as Version of record

Publication date:
2021

Link to publication in University of Groningen/UMCG research database

Citation for published version (APA):
Cohen-Sharir, Y., McFarland, J. M., Abdusamad, M., Marquis, C., Bernhard, S. V., Kazachkova, M., Tang, H., Ippolito, M. R., Laue, K., Zerbib, J., Malaby, H. L. H., Jones, A., Stautmeister, L-M., Bockaj, I., Wardenaar, R., Lyons, N., Nagaraja, A., Bass, A. J., Spierings, D. C. J., ... Ben-David, U. (2021). Aneuploidy renders cancer cells vulnerable to mitotic checkpoint inhibition. *Nature*, *590*(7846). https://doi.org/10.1038/s41586-020-03114-6

Article

Aneuploidy renders cancer cells vulnerable to mitotic checkpoint inhibition

Yael Cohen-Sharir[1], James M. McFarland[2], Mai Abdusamad[2], Carolyn Marquis[3], Sara V. Bernhard[4], Mariya Kazachkova[2], Helen Tang[2], Marica R. Ippolito[5], Kathrin Laue[1], Johanna Zerbib[1], Heidi L. H. Malaby[3], Andrew Jones[2], Lisa-Marie Stautmeister[4], Irena Bockaj[6], René Wardenaar[6], Nicholas Lyons[2], Ankur Nagaraja[2,7], Adam J. Bass[2,7], Diana C. J. Spierings[6], Floris Foijer[6], Rameen Beroukhim[2,7], Stefano Santaguida[5,8], Todd R. Golub[2,7], Jason Stumpff[3], Zuzana Storchová[4] & Uri Ben-David[1✉]

Selective targeting of aneuploid cells is an attractive strategy for cancer treatment[1]. However, it is unclear whether aneuploidy generates any clinically relevant vulnerabilities in cancer cells. Here we mapped the aneuploidy landscapes of about 1,000 human cancer cell lines, and analysed genetic and chemical perturbation screens[2–9] to identify cellular vulnerabilities associated with aneuploidy. We found that aneuploid cancer cells show increased sensitivity to genetic perturbation of core components of the spindle assembly checkpoint (SAC), which ensures the proper segregation of chromosomes during mitosis[10]. Unexpectedly, we also found that aneuploid cancer cells were less sensitive than diploid cells to short-term exposure to multiple SAC inhibitors. Indeed, aneuploid cancer cells became increasingly sensitive to inhibition of SAC over time. Aneuploid cells exhibited aberrant spindle geometry and dynamics, and kept dividing when the SAC was inhibited, resulting in the accumulation of mitotic defects, and in unstable and less-fit karyotypes. Therefore, although aneuploid cancer cells could overcome inhibition of SAC more readily than diploid cells, their long-term proliferation was jeopardized. We identified a specific mitotic kinesin, KIF18A, whose activity was perturbed in aneuploid cancer cells. Aneuploid cancer cells were particularly vulnerable to depletion of KIF18A, and KIF18A overexpression restored their response to SAC inhibition. Our results identify a therapeutically relevant, synthetic lethal interaction between aneuploidy and the SAC.

Aneuploidy, defined as copy number changes that encompass entire chromosome arms or whole chromosomes, is the most prevalent genetic alteration in human cancer[11,12] (Supplementary Note 1). As cancer cells are almost invariably aneuploid[12], whereas normal cells are (almost) always euploid[13], the identification of aneuploidy-targeting drugs has long been a goal of cancer research. Whereas aneuploidy-augmented cellular vulnerabilities have been described in yeast[14–17], they have not been systematically identified in human cancer. Large-scale studies are required to control for potentially confounding factors, and isogenic in vitro systems are needed to validate differential dependencies and dissect them mechanistically.

Sensitivity to genetic SAC perturbation

To identify cellular vulnerabilities associated with a high degree of aneuploidy, we evaluated the aneuploidy landscapes of 997 human cancer cell lines, using published copy number profiles from the Cancer Cell Line Encyclopedia (CCLE)[2]. Each cell line was assigned an 'aneuploidy score'[12,18] based on the number of chromosome arms gained or lost in

that cell line, relative to its basal ploidy (Fig. 1a, Extended Data Fig. 1a, Supplementary Table 1). We then analysed the association of aneuploidy with gene essentiality, using two distinct datasets of loss-of-function screens across 689 and 712 cell lines[3,4] (see Methods). Next, we performed a genome-wide comparison of the top (highly aneuploid; median 25 chromosome-arm alterations) and bottom (near-euploid; median 3 chromosome-arm alterations) cell line quartiles, in order to identify differential vulnerabilities (Fig. 1a); specifically, we searched for genes whose depletion was more lethal in highly aneuploid cell lines than in euploid (or near-euploid) ones.

We identified 263 and 64 differential dependencies of highly aneuploid cells in the RNAi-DRIVE and RNAi-Achilles datasets, respectively (Fig. 1b, Extended Data Fig. 1b, c, Supplementary Table 2, Supplementary Note 2). The list of genes that were preferentially essential in aneuploid cancer cells was highly enriched for cell-cycle-related pathways; in particular, the regulation of mitotic progression and the spindle assembly checkpoint (SAC; also known as the mitotic checkpoint) came up as the top preferentially essential pathways (Fig. 1c, Extended Data Fig. 1d, Supplementary Table 3). The genes that encode

[1]Department of Human Molecular Genetics and Biochemistry, Faculty of Medicine, Tel Aviv University, Tel Aviv, Israel. [2]Cancer Program, Broad Institute of MIT and Harvard, Cambridge, MA, USA. [3]Department of Molecular Physiology and Biophysics, University of Vermont, Burlington, VT, USA. [4]Department of Molecular Genetics, TU Kaiserlautern, Kaiserlautern, Germany. [5]Department of Experimental Oncology at IEO, European Institute of Oncology IRCCS, Milan, Italy. [6]European Research Institute for the Biology of Aging (ERIBA), University of Groningen, Groningen, The Netherlands. [7]Dana Farber Cancer Institute, Boston, MA, USA. [8]Department of Oncology and Hemato-Oncology, University of Milan, Milan, Italy. ✉e-mail: ubendavid@tauex.tau.ac.il
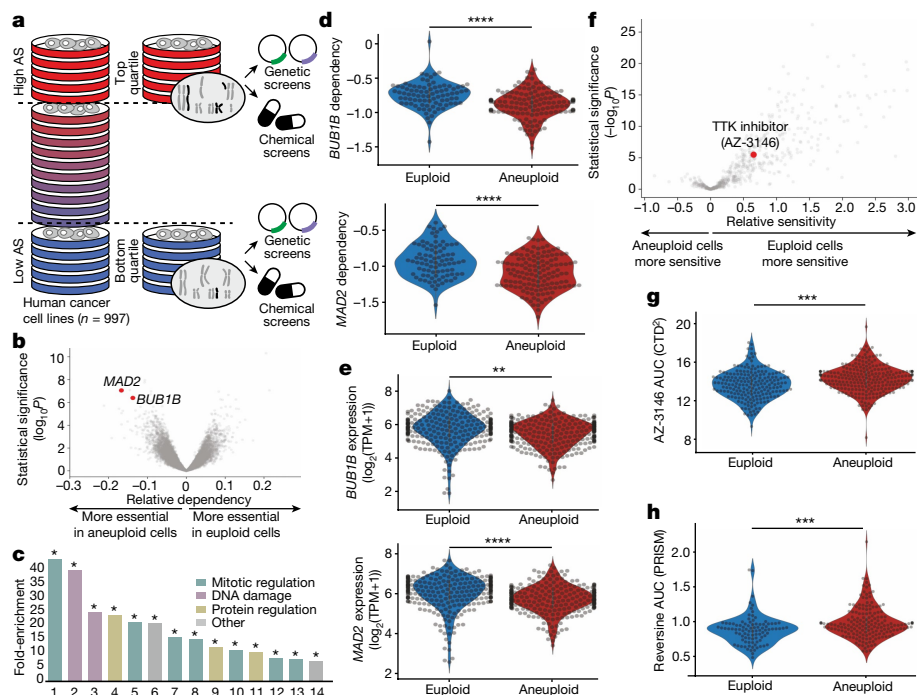
Fig. 1 | Differential sensitivity of aneuploid cancer cells to inhibition of the spindle assembly checkpoint. a, Schematics of our large-scale comparison of genetic and chemical dependencies between near-euploid and highly aneuploid cancer cell lines. Cell lines were assigned aneuploidy scores (AS), and the genetic and chemical dependency landscapes were compared between the top and bottom AS quartiles. **b**, The differential genetic dependencies between the near-euploid and highly aneuploid cancer cell lines (top versus bottom quartiles), based on the genome-wide Achilles RNAi screen. *BUB1B* and *MAD2* are highlighted in red. **c**, Pathways that were enriched in the list of genes that are more essential in highly aneuploid than in near-euploid cancer cell lines (effect size < −0.1, q < 0.1) in the Achilles RNAi screen. The full list is available in Supplementary Table 3. The most enriched pathway is the SAC. *P < 0.1; one-tailed Fisher's exact test, Benjamini corrected. **d**, The sensitivity of near-euploid and highly aneuploid cancer cell lines to knockdown of *BUB1B* (top) and *MAD2* (bottom) in the Achilles RNAi screen. The more negative a value, the more essential the gene is in that cell line. ****$P = 7 \times 10^{-7}$ and $P = 2 \times 10^{-7}$ for *BUB1B* and *MAD2*, respectively; two-tailed *t*-test. **e**, Comparison of mRNA expression of *BUB1B* (top) and *MAD2* (bottom) between near-euploid and highly aneuploid cancer cell lines. **$P = 0.001$, ****$P = 3 \times 10^{-6}$ for *BUB1B* and *MAD2*, respectively; two-tailed *t*-test. **f**, Differential drug sensitivities between the near-euploid and highly aneuploid cancer cell lines, based on the large-scale Cancer Target Discovery and Development (CTD²) drug screen. AZ-3146, the only SAC inhibitor in the screen, is highlighted in red. **g**, The sensitivity of near-euploid and highly aneuploid cancer cell lines to the SAC inhibitor AZ-3146 in the CTD² drug screen. AUC, area under the curve. ***$P = 2 \times 10^{-4}$; two-tailed *t*-test. **h**, The sensitivity of near-euploid and highly-aneuploid cancer cell lines to the SAC inhibitor reversine, as evaluated by the PRISM assay. ***$P = 3 \times 10^{-4}$; two-tailed *t*-test.

two core members of the SAC—*BUB1B* (also known as *BUBR1*) and *MAD2* (also known as *MAD2L1*)—were at the top of the 'hit' list (Fig. 1b, d, Extended Data Fig. 1b, e–g, Supplementary Table 2, Supplementary Note 3). Analysis of the Achilles CRISPR–Cas9 dataset[5] confirmed that highly aneuploid cell lines were more dependent on the SAC than were near-euploid cell lines ($P = 0.003$, $q = 0.1$; for the enrichment of the gene ontology (GO) term 'mitotic cell cycle checkpoint'). However, the association between aneuploidy and SAC essentiality was weaker in this dataset than in the RNAi-DRIVE and RNAi-Achilles datasets, consistent with the inability of most mammalian cells to tolerate complete SAC inactivation[19,20]. Further analysis showed that aneuploid cell lines exhibited a modest reduction in the mRNA and protein levels of both *BUB1B* and *MAD2* (Fig. 1e, Extended Data Fig. 1h), and that this lower expression was associated with greater sensitivity to genetic knockdown (Extended Data Fig. 1i–k, Supplementary Table 4, Supplementary Note 4). The other pathways that were more essential in aneuploid cells were the proteasome and the DNA damage response (Fig. 1c, Supplementary Table 3), two cellular processes that have been linked to the cellular response to aneuploidy[21].

We focused our downstream analyses on the SAC dependency, as it was the top differential vulnerability identified in our analysis, and also considering the following factors: first, the SAC has a key role in ensuring proper chromosome segregation during mitosis[10]; second, SAC perturbation leads to chromosomal instability, which results in aneuploid karyotypes and frequently also in tumour formation[22–27];

and third, inhibitors of the SAC regulator TTK (also known as MPS1) are currently being used in clinical trials, either as single agents or in combination with chemotherapy[28,29], but biomarkers of patients' responses to SAC inhibition remain unknown.

The degree of tumour aneuploidy is known to be associated with other genomic and cellular features, and in particular with tissue type, proliferation rate, chromosomal instability (CIN), whole genome duplication (WGD), and p53 function[12,30–35]. Indeed, all of these features strongly associated with the cancer cell line aneuploidy score (Extended Data Fig. 2a–e). Notably, however, the increased vulnerability of aneuploid cells to SAC perturbation remained robust when accounting for these (and additional) factors (Extended Data Fig. 3).

Sensitivity to chemical SAC perturbation

Next, we examined the association between aneuploidy and drug response, using three large-scale chemical screens[6–9]. As in the genetic analysis, we used the cell line aneuploidy score to compare drug sensitivity between the top and bottom aneuploidy quartiles (Fig. 1a). We found that aneuploid cell lines were more resistant to a short (3–5 days) exposure to a broad spectrum of drugs (Fig. 1f, Extended Data Fig. 4a, Supplementary Table 5).

BUB1B and MAD2 work together with multiple other proteins to execute the crucial role of the SAC during mitosis[36]. TTK is particularly critical for recruitment of the SAC to unattached kinetochores and for complex formation[37] (Supplementary Note 5). Aneuploid cancer

cells were less sensitive than euploid cells to the three TTK inhibitors included in the analysed chemical screens (Fig. 1f, g, Extended Data Fig. 4a, b, Supplementary Table 5), in apparent contrast to the findings of the genetic analysis. To confirm the chemical screen results, we validated that highly aneuploid cancer cell lines were more resistant than near-euploid cancer cell lines to the TTK inhibitor reversine[38] (Extended Data Fig. 4c).

We next performed a pooled screen of barcoded cell lines, using the PRISM platform[9], and examined the response to reversine in 578 adherent cancer cell lines (Supplementary Table 6). Indeed, highly aneuploid cells were significantly more resistant than near-euploid cells to a five-day treatment with reversine (Fig. 1h, Extended Data Fig. 4d, e, Supplementary Note 6).

SAC dependency evolves over time

The results above raised the question of why aneuploid cells exhibit increased sensitivity to genetic perturbation of SAC components, but reduced sensitivity to multiple TTK inhibitors. There are three potential explanations: 1) The degree of protein inhibition and/or the target specificity may differ between genetic and pharmacological perturbations. 2) Perturbation of distinct SAC components may have differential cellular consequences. 3) The viability effect may depend on the different assay time points; drug response was evaluated following 3–5 days of SAC inhibition, whereas the response to genetic perturbations was evaluated following more than 14 days of SAC inhibition, as these are the typical time points for chemical and genetic perturbation screens, respectively.

To resolve this conundrum, we turned to isogenic models of near-diploid cells with wild-type *TP53* and their highly aneuploid derivatives. We induced cytokinesis failure in HCT116 and RPE1 cells, thereby generating tetraploid cells that spontaneously became aneuploid[39] (termed HPT (HCT116-derived post-tetraploid) and RPT (RPE1-derived post-tetraploid)) (Extended Data Fig. 5a–c). These otherwise isogenic cell lines were exposed to two TTK inhibitors, reversine and MPI-0479605. The highly aneuploid derivatives were more resistant to both drugs in a five-day assay (Fig. 2a, Extended Data Fig. 6a), and this could not be explained by different proliferation rates or by general drug resistance (Extended Data Fig. 6b, c). Similarly, the highly aneuploid derivatives exhibited increased resistance to knockdown of *BUB1B*, *MAD2* and *TTK* mediated by small interfering RNA (siRNA) (Fig. 2b, Extended Data Fig. 6d). We obtained the same results with a subset of the near-euploid and highly aneuploid cancer cell lines used in the original screens (Extended Data Fig. 6e), as well as with an independent, distinct system of RPE1 cells and their aneuploid derivatives[40] (Fig. 2c, d, Extended Data Figs. 5d, 6f, Supplementary Note 7). Therefore, aneuploid cells exhibited short-term resistance to both genetic and chemical inhibition of all three SAC components.

To determine whether the differences between the genetic and chemical screens were due to the different time points of viability assessment, we followed the proliferation of HCT116 and HPT cells in response to prolonged genetic or chemical SAC inhibition. On day 5, siRNA-mediated knockdown of *BUB1B*, *MAD2* or *TTK* had a greater effect on the near-diploid HCT116 cells, consistent with the previous viability measurements; however, by day 14 of knockdown this trend had reversed, and the highly aneuploid HPT cells were more sensitive to SAC inhibition (Fig. 2e, Extended Data Fig. 7a). We observed the same reversal of relative sensitivity when we assessed long-term (14 days) versus short-term (5 days) cell viability following exposure to chemical TTK inhibitors (Fig. 2f, g, Extended Data Fig. 7b, c). The same was observed with the isogenic diploid/aneuploid RPE1 clones (Extended Data Fig. 7d), and with the near-diploid and highly aneuploid cancer cell lines (Extended Data Fig. 7e). Thus, the time point of viability assessment is critical for the results, explaining the apparent inconsistency between the genetic and chemical screens.
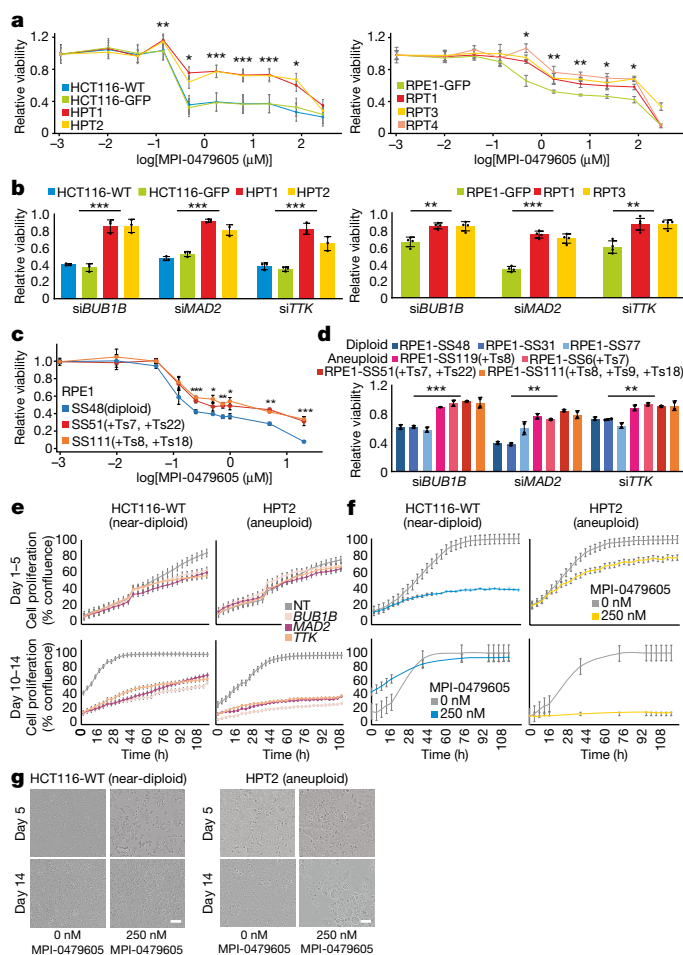

Fig. 2 | The effect of aneuploidy on cellular sensitivity to SAC inhibition in isogenic human cell lines. a, Dose–response curves of HCT116 and HPT cells (left), and RPE1 and RPT cells (right), to MPI-0479605 (120 h). Half-maximal effective concentration (EC_{50}) = 0.09 μM, 0.08 μM, 5.02 μM and 4.85 μM for HCT116-WT, HCT116-GFP, HPT1 and HPT2, respectively. EC_{50} = 0.16 μM, 1.48 μM, 1.52 μM and 3.31 μM, for RPE1-GFP, RPT1, RPT3 and RPT4, respectively. **b**, Responses of HCT116 and HPT cells (left; $n = 3$), and RPE1 and RPT cells (right; $n = 4$), to siRNA-mediated knockdown of *BUB1B*, *MAD2* or *TTK* (72 h). Results normalized to a non-targeting siRNA control. **c**, Dose–response curves of the near-diploid RPE1 clone SS48 and its isogenic aneuploid clones SS51 and SS111 to MPI-0479605 (120 h). EC_{50} = 0.02 μM, 0.08 μM and 0.04 μM, for SS48, SS51 and SS111, respectively. $n = 3$ for near-diploid and $n = 4$ for aneuploid clones. **d**, Response of three near-diploid and four aneuploid RPE1 clones to siRNA-mediated knockdown of *BUB1B*, *MAD2* or *TTK* (72 h). Results normalized to a non-targeting siRNA control. **e**, Proliferation curves of HCT116 and HPT cells cultured in the presence of siRNAs against *BUB1B*, *MAD2* or *TTK*, or a non-targeting (NT) control siRNA. **f**, Proliferation curves of HCT116 and HPT cells cultured in the presence of MPI-0479605 (250 nM) or DMSO control. **g**, Representative images of cells from **f**. Scale bars, 100 μm. Calculated doubling times for **e**, **f** are shown in Extended Data Fig. 7a, b. In all plots, data represent mean ± s.d. unless otherwise noted; $n = 3$ biological replicates in all experiments unless otherwise noted. *$P < 0.05$, **$P < 0.01$, ***$P < 0.001$; two-tailed t-test.

Cellular response to SAC inhibition

We next compared the expression changes induced by SAC inhibition in near-diploid and highly aneuploid cells (Fig. 3a, Extended Data Fig. 8a, Supplementary Table 7, Supplementary Note 8). The transcriptional responses to different SAC inhibitors were nearly identical within each cell line, and the two near-diploid parental cell lines clustered separately from the highly aneuploid derivatives (Fig. 3b). Gene set enrichment analysis (GSEA) revealed that negative regulation of cell cycle and positive regulation of cell death topped the differentially affected gene
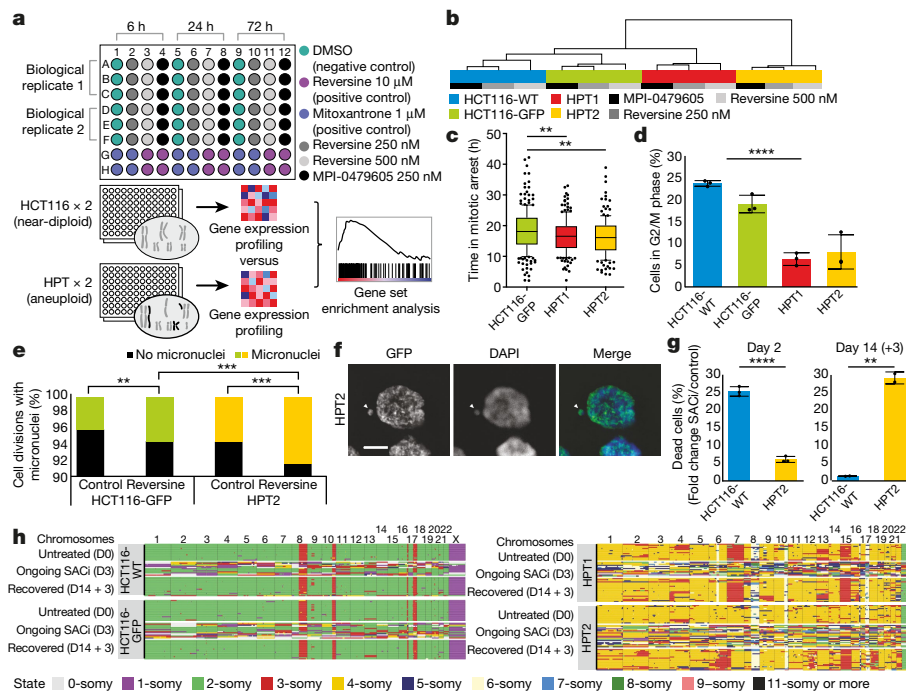
Fig. 3 | Transcriptional, cellular and karyotypic characterization of SAC inhibition in aneuploid cells. a, Schematics of gene expression profiling. HCT116 and HPT cells were treated with two SAC inhibitors, reversine (250 nM or 500 nM) and MPI-0479605 (250 nM), global gene expression profiles were generated at 6 h, 24 h and 72 h post-drug exposure, and gene set enrichment analysis was performed to compare the transcriptional effects of SAC inhibition (SACi). **b**, Unsupervised hierarchical clustering of the four cell lines based on drug-induced transcriptional changes. **c**, Time from mitotic arrest to division following treatment with nocodazole (200 ng ml^{-1}). **P < 0.01; two-tailed t-test. Bar, median; box, 25th and 75th percentiles; whiskers, 1.5× interquartile range (IQR); circles, individual cells. **d**, Flow cytometry-based quantification of G2/M phase arrest induced by 48-h exposure to MPI-0479605 (250 nM). ****P = 1×10^{-5}; two-tailed t-test. **e**, Prevalence of micronucleus formation in HCT116 and HPT cells cultured under standard conditions or

exposed to reversine (500 nM) for 24 h. **P = 0.007, ***P < 0.001; two-tailed Fisher's exact test. **f**, Representative images of micronucleus formation (arrowheads) in HPT2 cells exposed to reversine (500 nM) for 24 h. Scale bar, 10 μm. **g**, Flow cytometry-based quantification of sub-G1 cell fraction induced by 48 h (left) or 14 days (+ 3 days recovery; right) exposure to MPI-0479605 (250 nM). **P = 0.002, ****P = 3×10^{-5}; two-tailed t-test. **h**, Genome-wide copy number profiles of HCT116 and HPT single cells, as generated by the AneuFinder algorithm, at baseline (untreated; day 0 (D0)), after 3 days of MPI-0479605 (250 nM) treatment (ongoing SACi; D3), and after recovery from 14 days of treatment (recovered; D14 + 3). Individual cells are represented as rows, with chromosomes plotted as columns. In all plots, data represent the mean ± s.d. unless otherwise noted; n = 3 biological replicates in all experiments unless otherwise noted.

sets (Extended Data Fig. 8b, c). These findings suggest that three days after drug exposure, although the highly aneuploid cells seem to be more resistant than their near-diploid counterparts, they have already begun to downregulate cell cycle and upregulate cell death pathways that will ultimately lead to their elimination.

Thus, we hypothesized that aneuploid cancer cells overcame SAC inhibition more readily than diploid cells, but consequently acquired severe aberrations that jeopardized their survival and proliferation. Indeed, the HPT cells overcame mitotic arrest faster after exposure to the microtubule-depolymerizing drug nocodazole (Fig. 3c). When treated with a SAC inhibitor, the induction of cell cycle arrest and the decrease in the mitotic index were weaker in HPT cells than in HCT116 cells (Fig. 3d, Extended Data Fig. 8d). Furthermore, SAC inhibition in HPT cells resulted in a significant increase in mitotic aberrations, such as multipolar cell divisions, formation of micronuclei and failure of cytokinesis (Fig. 3e, f, Extended Data Fig. 8e–g). Consequently, SAC inhibition initially induced more cell death in HCT116 cells than in HPT cells, but prolonged drug exposure ultimately resulted in much more cell death within the aneuploid cultures (Fig. 3g). We obtained very similar results with RPE1 cells and their highly aneuploid RPT derivatives (Extended Data Fig. 8h–j). These results confirm that highly aneuploid cells can overcome SAC inhibition more readily than their parental near-diploid cells, resulting in the accumulation of a variety of mitotic aberrations and eventually in their death.

Karyotype evolution after SAC inhibition

We next characterized the karyotype composition of the HCT116 and HPT cell lines before, during and after SAC inhibition. We used single-cell DNA sequencing[41] to karyotype a total of 210 single cells across two near-diploid (HCT116-WT and HCT116-GFP) and two highly aneuploid (HPT1 and HPT2) lines at three time points—before treatment (day 0); following short-term SAC inhibition (day 3); and after recovery from long-term exposure (day 14 + 3).

Before treatment, both karyotypic heterogeneity and the degree of aneuploidy were higher in the HPT populations, as expected (Fig. 3h, Extended Data Fig. 8k, l). Three days of SAC inhibition induced CIN in all lines, but the resulting karyotypic heterogeneity was significantly higher in HPT cells (P = 2×10^{9}; Extended Data Fig. 8k–m), consistent with the increased prevalence of mitotic aberrations in these cells. In the near-diploid populations, the cells that survived prolonged drug treatment had the same near-diploid karyotype—and low degree of karyotypic heterogeneity—as the untreated cells (Fig. 3h, Extended Data Fig. 8k, l), suggesting that the original near-diploid karyotype was fitter than the aneuploid karyotypes induced by the drug. By contrast, in the aneuploid populations, the (fewer) surviving cells had highly aneuploid and heterogeneous karyotypes. Several aneuploidies became more prevalent following treatment, but these events were not shared between the two HPT clones (Fig. 3h, Extended Data Fig. 8k, l). Therefore, there was no evidence for selection for one specific karyotype in the treated HPT cells.
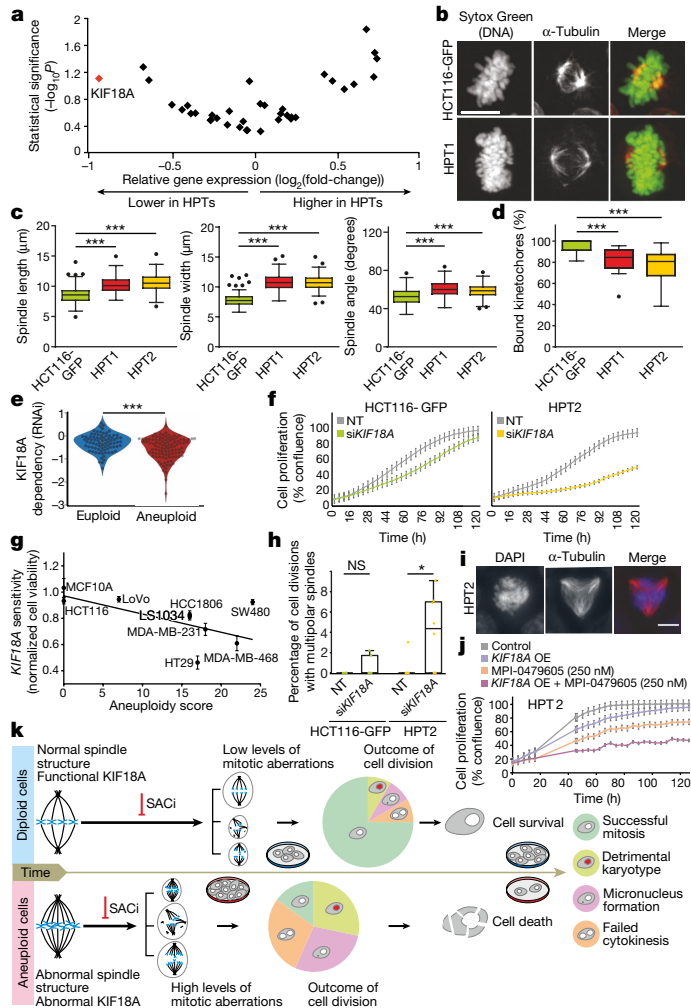
Fig. 4 | Altered spindle geometry and dynamics, and increased dependency on the mitotic kinesin KIF18A, in aneuploid cancer cells. a, HCT116 and HPT cell lines show differential mRNA expression of mitotic kinesins. *KIF18A* is highlighted in red. **b**, Imaging of metaphase spindle in HCT116-GFP and HPT1 cells. Scale bar, 10 μm. (**c**) Spindle length (left), width (middle), and angle (right) in HCT116 and HPT cells. The definitions of length, width and angle are shown in Extended Data Fig. 9c. ***P < 0.001; two-tailed *t*-test. **d**, The percentage of spindle microtubule-bound kinetochores in HCT116 and HPT cells. ***P < 0.001; two-tailed *t*-test. **e**, Sensitivity of near-euploid and highly aneuploid cancer cell lines to knockdown of *KIF18A* in the RNAi-DRIVE dataset. The more negative a value, the more essential the gene is in that cell line. ***P = 3 × 10^{-4}; two-tailed *t*-test. **f**, Proliferation curves of HCT116-GFP and HPT2 cells cultured in the presence of a *KIF18A*-targeting siRNA or a non-targeting (NT) control siRNA. **g**, The sensitivity of cancer cell lines to the knockdown of *KIF18A* as a function of their aneuploidy score. Spearman's *ρ* = −0.66 (*P* = 0.026; one-tailed test). **h**, The prevalence of cell divisions with multipolar spindles in HCT116 and HPT2 cells treated with *KIF18A*-targeting siRNA or a non-targeting siRNA. NS, *P* > 0.05, *P = 0.03; two-tailed *t*-test. **i**, Representative images of multipolar spindles in HPT2 cells following siRNA-mediated *KIF18A* knockdown. Scale bar, 10 μm. **j**, Proliferation curves of HPT2 cells before and after overexpression (OE) of *KIF18A* in the absence or presence of MPI-0479605 (250 nM). Overexpression of *KIF18A* restores the inhibitory effect of SAC inhibition. **k**, A model of the evolving response of aneuploid cancer cells to SAC inhibition (SACi). For more details, see Supplementary Note 12. In all plots, data represent the mean ± s.d. unless otherwise noted; *n* = 3 biological replicates in all experiments. Box plots: bar, median; box, 25th and 75th percentiles; whiskers, 1.5 × IQR; circles, individual data points.

We conclude that SAC inhibition induces lower levels of CIN in surviving near-diploid cells, enabling the selection of cells that preserve the original near-diploid karyotype; by contrast, highly aneuploid cells experience a higher degree of CIN, and cannot readily select for a fit karyotype that would enable their long-term survival.

Spindle alterations in aneuploid cells

To study the molecular underpinning of the differing responses to SAC inhibition, we analysed the changes in spindle proteins in the HPT and RPT cells compared to their parental cell lines. The mRNA and protein expression levels of one specific mitotic kinesin, KIF18A, were reduced in the HPT cells (Fig. 4a, Extended Data Fig. 9a, b). Notably, depletion of KIF18A alters the spindle geometry, making the spindle longer and wider[42,43], and *KIF18A* knockdown decreases kinetochore–microtubule stability in HCT116 cells[44]. The HPT cells exhibited similarly altered spindle geometry: spindle length, width and angle were all significantly higher in the HPT cells than in their near-diploid parental cells (Fig. 4b, c, Extended Data Fig. 9c). These structural changes were associated with alterations in spindle activity: microtubule polymerization rate, EB1α-tubulin co-localization and microtubule–kinetochore attachments were significantly reduced in the HPT cells (Fig. 4d, Extended Data Fig. 9d, e). Thus, highly aneuploid cells exhibited altered spindle geometry and dynamics.

Therefore, we hypothesized that aneuploid cells might also be more dependent on KIF18A function than near-euploid cells. To test this hypothesis, we turned back to our large-scale genomic analysis of cancer cell lines (Supplementary Table 2). Indeed, highly aneuploid cancer cells were significantly more sensitive to *KIF18A* knockdown or knockout compared to near-euploid cancer cells (Fig. 4e, Extended Data Figs. 9f, g, 10a–i, Supplementary Note 9), although there was no significant difference in mRNA or protein expression of KIF18A between the groups (Extended Data Fig. 9h–k, Supplementary Note 10, Supplementary Table 8). KIF18A was the only differentially essential kinesin in our analysis (out of 42 kinesins tested), and ranked eleventh overall on the list of genes that were most preferentially essential in aneuploid cancer cells in the RNAi-DRIVE dataset (Supplementary Table 2).

We confirmed that the aneuploid cells were more sensitive to *KIF18A* depletion using siRNA-mediated knockdown in HCT116 and HPT cells (Fig. 4f, Extended Data Fig. 9l–n). Moreover, sensitivity to *KIF18A* depletion[45] strongly correlated with aneuploidy score across a panel of nine cancer cell lines (Spearman's *ρ* = −0.66, *P* = 0.026; Fig. 4g). Live-cell imaging identified a modest mitotic delay in HPT cells following siRNA-mediated *KIF18A* knockdown (Extended Data Fig. 9o), followed by a significant increase in multipolar cell divisions (Fig. 4h, i) and formation of micronuclei (Extended Data Fig. 9p); by contrast, KIF18A depletion in the near-diploid HCT116 cells did not lead to similarly severe aberrations (Fig. 4h, Extended Data Fig. 9o, p). We obtained similar results with the RPE1 cells and their highly aneuploid RPT derivatives (Extended Data Fig. 10j–n). Consistent with these results, other studies now report increased sensitivity to *KIF18A* perturbation in chromosomally unstable aneuploid cell lines[45] and aneuploid WGD^{+} cell lines[46].

Last, we examined whether the observed differential sensitivities of aneuploid cells to SAC inhibition and KIF18A depletion were functionally related. We overexpressed KIF18A in HPT cells (Extended Data Fig. 9q) and examined their sensitivity to SAC inhibition. Whereas KIF18A overexpression alone had a minimal effect on cell viability and proliferation, it sensitized the aneuploid cells to short-term SAC inhibition (Fig. 4j, Extended Data Fig. 9r). This 'phenotypic rescue' experiment demonstrates a causal link between KIF18A and cellular sensitivity to SAC inhibition. Further study is required to elucidate the nature of this interaction at the molecular level.

Discussion

The potential of targeting aneuploid cells to selectively kill cancer cells remains unfulfilled. Here, we assigned aneuploidy scores to about 1,000

Article

cancer cell lines, performed a comprehensive analysis of large-scale genetic and chemical perturbation screens, and found that aneuploid cancer cells show increased dependency on the SAC core members BUB1B and MAD2 (Supplementary Note 11). Using a subset of ten cancer cell lines, as well as three model systems of isogenic near-diploid and aneuploid cell lines, we confirmed the increased vulnerability of aneuploid cells to SAC inhibition. Transcriptional profiling, flow cytometry, single-cell DNA sequencing and imaging-based analyses of mitosis revealed an altered response of aneuploid cells to SAC inhibition. Finally, we found that the mitotic kinesin gene *KIF18A* was preferentially essential in aneuploid cells and functionally related to their increased dependency on SAC activity.

Our findings reveal that aneuploid cells can initially overcome SAC inhibition more readily than diploid cells; however, the resultant aberrant cells exhibit severe viability and proliferation defects (Fig. 4k, Supplementary Note 12). These findings may have several important implications for the clinical use of TTK inhibitors, as they suggest that aneuploidy may serve as a biomarker for predicting drug response to this class of drugs, highlight the value of testing such drugs over a longer time course, and identify a potential need to develop selective inhibitors of BUB1B and MAD2 (Supplementary Note 13). In addition, the increased sensitivity of aneuploid cancer cells to KIF18A inhibition is interesting per se, given the attempts to develop highly selective and bioactive KIF18A inhibitors[47] (Supplementary Notes 13–15).

Finally, our large-scale analyses revealed additional candidate vulnerabilities that deserve experimental validation (for example, increased sensitivity to proteasome inhibition; Supplementary Table 3). Furthermore, our characterization of aneuploidy profiles and scores across the CCLE lines (Supplementary Table 1) will be useful for the identification of additional genomic features and cellular vulnerabilities associated with high degree of aneuploidy or with specific recurrent aneuploidies. To facilitate further interrogation of this resource, we have integrated the cell line aneuploidy profiles and scores into the DepMap portal (https://depmap.org/portal/). We hope that this study will pave the way for the routine integration of aneuploidy status in the genomic analysis of cancer dependencies.

Online content

Any methods, additional references, Nature Research reporting summaries, source data, extended data, supplementary information, acknowledgements, peer review information; details of author contributions and competing interests; and statements of data and code availability are available at https://doi.org/10.1038/s41586-020-03114-6.

1. Ben-David, U. & Amon, A. Context is everything: aneuploidy in cancer. *Nat. Rev. Genet.* **21**, 44–62 (2020).
2. Ghandi, M. et al. Next-generation characterization of the Cancer Cell Line Encyclopedia. *Nature* **569**, 503–508 (2019).
3. Tsherniak, A. et al. Defining a cancer dependency map. *Cell* **170**, 564–576.e16 (2017).
4. McDonald, E. R. III et al. Project DRIVE: a compendium of cancer dependencies and synthetic lethal relationships uncovered by large-scale, deep RNAi screening. *Cell* **170**, 577–592.e10 (2017).
5. Aguirre, A. J. et al. Genomic copy number dictates a gene-independent cell response to CRISPR/Cas9 targeting. *Cancer Discov.* **6**, 914–929 (2016).
6. Yang, W. et al. Genomics of Drug Sensitivity in Cancer (GDSC): a resource for therapeutic biomarker discovery in cancer cells. *Nucleic Acids Res.* **41**, D955–D961 (2013).
7. Basu, A. et al. An interactive resource to identify cancer genetic and lineage dependencies targeted by small molecules. *Cell* **154**, 1151–1161 (2013).
8. Garnett, M. J. et al. Systematic identification of genomic markers of drug sensitivity in cancer cells. *Nature* **483**, 570–575 (2012).
9. Corsello, S. M. et al. Discovering the anticancer potential of non-oncology drugs by systematic viability profiling. *Nat. Cancer* **1**, 235–248 (2020).
10. Musacchio, A. & Salmon, E. D. The spindle-assembly checkpoint in space and time. *Nat. Rev. Mol. Cell Biol.* **8**, 379–393 (2007).
11. Zack, T. I. et al. Pan-cancer patterns of somatic copy number alteration. *Nat. Genet.* **45**, 1134–1140 (2013).
12. Taylor, A. M. et al. Genomic and functional approaches to understanding cancer aneuploidy. *Cancer Cell* **33**, 676–689.e3 (2018).
13. Knouse, K. A., Wu, J., Whittaker, C. A. & Amon, A. Single cell sequencing reveals low levels of aneuploidy across mammalian tissues. *Proc. Natl Acad. Sci. USA* **111**, 13409–13414 (2014).
14. Oromendia, A. B., Dodgson, S. E. & Amon, A. Aneuploidy causes proteotoxic stress in yeast. *Genes Dev.* **26**, 2696–2708 (2012).
15. Torres, E. M. et al. Effects of aneuploidy on cellular physiology and cell division in haploid yeast. *Science* **317**, 916–924 (2007).
16. Hwang, S. et al. Serine-dependent sphingolipid synthesis is a metabolic liability of aneuploid cells. *Cell Rep.* **21**, 3807–3818 (2017).
17. Storchová, Z. et al. Genome-wide genetic analysis of polyploidy in yeast. *Nature* **443**, 541–547 (2006).
18. Ben-David, U. et al. Patient-derived xenografts undergo mouse-specific tumor evolution. *Nat. Genet.* **49**, 1567–1575 (2017).
19. Kops, G. J. P. L., Foltz, D. R. & Cleveland, D. W. Lethality to human cancer cells through massive chromosome loss by inhibition of the mitotic checkpoint. *Proc. Natl Acad. Sci. USA* **101**, 8699–8704 (2004).
20. Wild, T. et al. The spindle assembly checkpoint is not essential for viability of human cells with genetically lowered APC/C activity. *Cell Rep.* **14**, 1829–1840 (2016).
21. Chunduri, N. K. & Storchová, Z. The diverse consequences of aneuploidy. *Nat. Cell Biol.* **21**, 54–62 (2019).
22. Baker, D. J., Jin, F., Jeganathan, K. B. & van Deursen, J. M. Whole chromosome instability caused by Bub1 insufficiency drives tumorigenesis through tumor suppressor gene loss of heterozygosity. *Cancer Cell* **16**, 475–486 (2009).
23. Ricke, R. M., Jeganathan, K. B. & van Deursen, J. M. Bub1 overexpression induces aneuploidy and tumor formation through Aurora B kinase hyperactivation. *J. Cell Biol.* **193**, 1049–1064 (2011).
24. Foijer, F. et al. Chromosome instability induced by Mps1 and p53 mutation generates aggressive lymphomas exhibiting aneuploidy-induced stress. *Proc. Natl Acad. Sci. USA* **111**, 13427–13432 (2014).
25. Foijer, F. et al. Deletion of the *MAD2L1* spindle assembly checkpoint gene is tolerated in mouse models of acute T-cell lymphoma and hepatocellular carcinoma. *eLife* **6**, e20873 (2017).
26. Sotillo, R. et al. Mad2 overexpression promotes aneuploidy and tumorigenesis in mice. *Cancer Cell* **11**, 9–23 (2007).
27. Sotillo, R., Schvartzman, J. M., Socci, N. D. & Benezra, R. Mad2-induced chromosome instability leads to lung tumour relapse after oncogene withdrawal. *Nature* **464**, 436–440 (2010).
28. Mason, J. M. et al. Functional characterization of CFI-402257, a potent and selective Mps1/TTK kinase inhibitor, for the treatment of cancer. *Proc. Natl Acad. Sci. USA* **114**, 3127–3132 (2017).
29. Pauer, L. R. et al. Phase I study of oral CI-994 in combination with carboplatin and paclitaxel in the treatment of patients with advanced solid tumors. *Cancer Invest.* **22**, 886–896 (2004).
30. Bielski, C. M. et al. Genome doubling shapes the evolution and prognosis of advanced cancers. *Nat. Genet.* **50**, 1189–1195 (2018).
31. Carter, S. L. et al. Absolute quantification of somatic DNA alterations in human cancer. *Nat. Biotechnol.* **30**, 413–421 (2012).
32. Hieronymus, H. et al. Tumor copy number alteration burden is a pan-cancer prognostic factor associated with recurrence and death. *eLife* **7**, e37294 (2018).
33. Smith, J. C. & Sheltzer, J. M. Systematic identification of mutations and copy number alterations associated with cancer patient prognosis. *eLife* **7**, e39217 (2018).
34. Soto, M., García-Santisteban, I., Krenning, L., Medema, R. H. & Raaijmakers, J. A. Chromosomes trapped in micronuclei are liable to segregation errors. *J. Cell Sci.* **131**, jcs214742 (2018).
35. Zhang, C. Z. et al. Chromothripsis from DNA damage in micronuclei. *Nature* **522**, 179–184 (2015).
36. Burgess, A., Rasouli, M. & Rogers, S. Stressing mitosis to death. *Front. Oncol.* **4**, 140 (2014).
37. Dominguez-Brauer, C. et al. Targeting mitosis in cancer: emerging strategies. *Mol. Cell* **60**, 524–536 (2015).
38. Santaguida, S., Tighe, A., D'Alise, A. M., Taylor, S. S. & Musacchio, A. Dissecting the role of MPS1 in chromosome biorientation and the spindle checkpoint through the small molecule inhibitor reversine. *J. Cell Biol.* **190**, 73–87 (2010).
39. Kuznetsova, A. Y. et al. Chromosomal instability, tolerance of mitotic errors and multidrug resistance are promoted by tetraploidization in human cells. *Cell Cycle* **14**, 2810–2820 (2015).
40. Santaguida, S. et al. Chromosome mis-segregation generates cell-cycle-arrested cells with complex karyotypes that are eliminated by the immune system. *Dev. Cell* **41**, 638–651.e5 (2017).
41. Bakker, B. et al. Single-cell sequencing reveals karyotype heterogeneity in murine and human malignancies. *Genome Biol.* **17**, 115 (2016).
42. Weaver, L. N. et al. Kif18A uses a microtubule binding site in the tail for plus-end localization and spindle length regulation. *Curr. Biol.* **21**, 1500–1506 (2011).
43. Czechanski, A. et al. Kif18a is specifically required for mitotic progression during germ line development. *Dev. Biol.* **402**, 253–262 (2015).
44. Wordeman, L., Decarreau, J., Vicente, J. J. & Wagenbach, M. Divergent microtubule assembly rates after short- versus long-term loss of end-modulating kinesins. *Mol. Biol. Cell* **27**, 1300–1309 (2016).
45. Marquis, C. et al. Chromosomally unstable tumor cells specifically require KIF18A for proliferation. *Nat. Comm.* (in the press).
46. Quinton, R. J. et al. Whole-genome doubling confers unique genetic vulnerabilities on tumour cells. *Nature* https://doi.org/10.1038/s41586-020-03133-3 (2021).
47. Braun, J. et al. Synthesis and biological evaluation of optimized inhibitors of the mitotic kinesin Kif18A. *ACS Chem. Biol.* **10**, 554–560 (2015).

Methods

No statistical methods were used to predetermine sample size. The experiments were not randomized and the investigators were not blinded to allocation during experiments and outcome assessment.

Aneuploidy score assignment

Aneuploidy was quantified by estimating the total number of arm-level gains and losses for each cell line, based on the published ABSOLUTE copy number data of the CCLE dataset[2]. The median total modal copy number (sum of allelic copy numbers) across segments was estimated for each chromosome arm (weighted for segment length), and compared to the cell line's background ploidy in order to call the chromosome-arm copy number status (gain, loss or neutral). Aneuploidy score (AS) was defined as the total number of chromosome arms that were gained or lost. The cell lines with bottom-quartile AS (corresponding to cell lines with a median of three chromosome-arm copy number changes; min = 0, max = 7) were defined as the 'near-euploid' group, and the cell lines with the top-quartile AS (corresponding to cell lines with a median of 25 chromosome-arm copy number changes; min = 22, max = 36) were defined as the 'highly aneuploid' group.

Association of aneuploidy with genomic and phenotypic features

Cell line doubling time measurements were obtained from Tsherniak et al.[3]. The mutation calls and mRNA expression levels were obtained from the CCLE mutation and gene expression data sets (19q4 DepMap release; CCLE_mutations.csv and CCLE_expression_full.csv, respectively)[2]. The genetic perturbation data sets used were the gene_effect files from RNAi Achilles[48], RNAi DRIVE[48], and CRISPR Achilles (19q4 DepMap release). RNAi data are available at https://doi.org/10.6084/m9.figshare.6025238.v4 and CRISPR, mutation, and expression data are available at https://doi.org/10.6084/m9.figshare.11384241.v2. The chemical perturbation data sets used were the PRISM Repurposing Secondary Screen[9], CTD[2] (refs. [49,50]), and GDSC[51]. Normalized protein abundance measurements across cell lines were obtained from Nusinow et al.[52]. Cell line microsatellite instability was determined using next-generation sequencing and PCR-based phenotyping, obtained from Chan et al.[53] Cell lines were split into two groups: the top and bottom quartiles of AS. Genes that were preferentially essential in highly aneuploid compared to near-euploid cell lines were identified by linear modelling performed in parallel across genes using the R package Limma[54]. The difference in mean dependency between the groups was evaluated for each gene, and associated P values were derived from empirical-Bayes-moderated t-statistics. q values were computed using the Benjamini–Hochberg method[55]. This process was repeated with various features of the cell lines (cell lineage, karyotype heterogeneity (HET70) score[56] or doubling time) included as a covariate. To remove the effects of confounding variables (cell lineage, HET70 or doubling time), we fit linear regression models (Scikit-learn)[57] and computed the residuals, maintaining the across-cell line average dependency scores fixed. To test mRNA expression as a predictor of genetic perturbation of *BUB1B* and *MAD2*, we fit linear regression models using the lm function from R Stats Package[58], including lineage annotations as co-variates.

Association between common essential genes and drug response

Chemical perturbation log fold-change data from the PRISM Repurposing Primary Screen[9] were correlated with the respective annotated drug targets in the genetic perturbation data. Log fold-change data were calculated relative to DMSO, and ComBat was used to correct for experimental confounders, as described[9]. Common essential genes were defined as on DepMap (https://depmap.org/portal/).

Functional enrichment analysis

The list of differentially-essential genes between the near-euploid and highly aneuploid groups (effect size < −0.1, q < 0.1) was subjected to a DAVID functional annotation enrichment analysis[59], focusing on the GO Biological Process gene sets. The full list of genes included in each screen was used as background.

Reversine biomarker analysis

The scikit-learn's RandomForestRegressor[57] was used to predict Reversine AUC values for 502 cell lines. The input features were (19Q4 release): RNA sequencing expression data for both protein-coding and non-coding regions (CCLE_expression_full.csv); mutation statuses, broken into three binary matrices: damaging, hotspot and other (CCLE_mutations.csv); and gene level copy number (CCLE_gene_cn.csv). Data are available at https://doi.org/10.6084/m9.figshare.11384241.v2. As previously described[60], we used tenfold cross-validation, filtered features to the 1,000 that had the highest Pearson correlation with the Reversine AUC values in the training set, and reported accuracy via Pearson correlation between the measured AUC values and the complete set of out-of-sample predictions. To estimate feature importance values we retrained the model on all the samples and used RandomForestRegressor's feature_importances_attribute. This attribute is a measure of the average contribution of a feature to decreasing the variance when splitting values at nodes.

Generation of isogenic near-diploid and highly aneuploid cell lines

The HPT and RPT aneuploid derivatives were generated from the near-diploid human colorectal cancer cell line HCT116, and from the human immortalized retinal pigment epithelium cell line RPE1, respectively. The cells were treated with dihydrocytochalasin D for 18 h, washed in Dulbecco's modified Eagle's medium (DMEM) and cloned by limiting dilution to obtain single-cell clones within 30 days. Individual clones were then screened by flow cytometry for DNA content and near-tetraploid cell lines were validated via metaphase spreads. Selected clones were further characterized by multicolour fluorescent in situ hybridization (FISH) karyotyping and by single nucleotide polymorphism (SNP) array profiling, which showed that the cell lines were not stable as tetraploid, but were chromosomally unstable, and quickly became highly aneuploid, mostly through chromosome loss. The characterized cell lines were expanded and stored in liquid nitrogen. Cells were propagated for a maximum of five additional passages before being used in experiments. Further description is available in the original report of their derivation[39]. Chromosome count, based on a standard karyotypic analysis of the HCT116 and HPT cell lines, is shown in Extended Data Fig. 5b, c.

To generate cell lines harbouring stable aneuploid karyotypes (and euploid controls), we transiently treated RPE1-hTERT cells with the TTK inhibitor reversine (500 nM, 24 h) to induce random chromosome gains and losses (aneuploid population), or with a vehicle control (for the euploid population). After drug wash-out, euploid and aneuploid populations were single-cell sorted in 384-well plates (FACSAria, BD Biosciences), expanded, and their karyotypes assessed by bulk DNA sequencing. The karyotypic analysis of the RPE1-SS clones is shown in Extended Data Fig. 5d.

Cell culture

HCT116 and RPE1 cells, their aneuploid derivatives HPT and RPT, MDAMB468, A101D, EN, VMCUB1, CAL51 and SW48 cells were cultured in DMEM (Life Technologies) with 10% fetal bovine serum (Sigma-Aldrich) and 1% penicillin-streptomycin-glutamine (Life Technologies). SH10TC, NCIH1693, MHHNB11 and PANC0813 cells were cultured in RPMI-1640 (Life Technologies) with 10% fetal bovine serum (Sigma-Aldrich) and 1% penicillin-streptomycin-glutamine (Life Technologies). PANC0813 medium was supplemented with 10 U/ml human recombinant insulin (Sigma-Aldrich), and MHHNB11 medium was supplemented with MEM Non-Essential Amino Acids (Sigma-Aldrich). Cells were incubated at 37 °C with 5% CO_2 and passaged twice a week using Trypsin-EDTA (0.25%)

Article

(Life Technologies). Cells were tested for mycoplasma contamination using the MycoAlert Mycoplasma Detection Kit (Lonza), according to the manufacturer's instructions.

PRISM screening

The PRISM screen was performed as described[9]. In brief, barcoded cell lines were pooled (25 cell lines per pool) based on doubling time and frozen into assay-ready vials. Vials were thawed and one pool was immediately plated in 384-well plate at 1,250 cells per well in triplicate. Twenty-four hours later, cells were plated onto assay ready plates containing eight different concentrations of reversine (threefold dilutions ranging from 0.9 nM to 20 μM) or control DMSO. Five days later, cells were lysed, and lysate plates were then pooled for amplification and barcode measurement. Viability values were calculated by taking the median fluorescence intensity of beads corresponding to each cell line barcode, and normalizing them by the median of DMSO control treatments. High-quality viability measurements could be generated for 530 cell lines. Dose–response curves were calculated by fitting four-parameter curves to viability data for each compound and cell line using the R package drc and fixing the upper asymptote of the logistic curves to 1; the area under the dose–response curve (AUC) values were calculated using a normalized integral[9] (Supplementary Table 6).

Cell growth rate analysis

Kinetic cell proliferation assays were monitored using the IncuCyte S3 Live Cell Analysis System (Essen Bioscience). Ninety-six-well plates were incubated at 37 °C with 5% CO_2. Four non-overlapping planes of view phase contrast images were captured using a 10× objective, with data collected every 4 h for the duration of each experiment. IncuCyte Base Software was used to calculate average confluence. Population doublings were calculated using the formula $T_{doubling} = (\log_2(\Delta T))/(\log(c_2) - \log(c_1))$, where c_1 and c_2 are the minimum and maximum percentage confluences during the linear growth phase, respectively, and ΔT is the time elapsed between c_1 and c_2. Cell masking in representative images was done for visualization purposes, using ilastik image analysis software[61].

Drug response assays

For drug experiments, cells were plated at 1×10^4 cells per well and treated with compounds 24 h later. MPI-0479605 was purchased from MedChem Express, and reversine and mitoxantrone were purchased from Sigma-Aldrich. For prolonged drug exposure (14 days or longer), cells were split as necessary, so that all control cells were split at the same time, and all treated cells were split at the same time. Cells were allowed to recover before drugs were replenished, and day count was based on the total number of days in the presence of the drug (for example, D14 corresponds to 14 days of drug exposure). Following incubation with the drug, viability was assessed either by live-cell imaging using the IncuCyte S3 Live Cell Analysis System (Essen Bioscience) or using CellTiter-Glo (Promega) or crystal violet staining (Sigma). Luminescence and absorbance were quantified using an Envision Plate Reader (PerkinElmer). Experiments were performed in triplicate, averaged and normalized to negative (DMSO-matched) controls. EC_{50} values were calculated in GraphPad Prism using an asymmetric (five parameters) nonlinear regression model.

Cell transfections

Cells were seeded in 100 μl medium in black, clear-bottom 96-well plates (Corning 3904) excluding edge wells at 5×10^3 cells per well one day before transfections. For siRNA experiments, cells were transfected with 25 nM siRNA against *BUB1B*, *MAD2L1*, *TTK* or *KIF18A*, or a non-targeting control (Dharmacon ON-TARGETplus SMARTpool) in triplicate using DharmaFECT 1 Transfection Reagent (Dharmacon) as per the manufacturer's protocol. For prolonged siRNA exposure (14 days or longer), cells were split as necessary, so that all control cells were split at the same time, and all treated cells were split at the same time. Cells were allowed to recover before siRNAs were replenished, and day count was based on the total number of days in the presence of the siRNA (for example, D14 corresponds to 14 days of siRNA exposure). For *KIF18A* overexpression experiments, cells were transfected with 100 ng pMX229, a gift from Linda Wordeman (Addgene plasmid #23002), using TransIT-LT1 Transfection Reagent (Mirus). For combination experiments with SAC inhibitors, cells were transfected and treated with drugs simultaneously. Following incubation with the siRNAs, the overexpressing vector and/or the drugs, viability was assessed either by live-cell imaging using the IncuCyte S3 Live Cell Analysis System (Essen Bioscience) or using CellTiter-Glo (Promega). Luminescence was measured using an Envision Plate Reader (PerkinElmer). Experiments were performed in triplicate, averaged and normalized to negative (DMSO-matched) control.

RNA extraction and real-time quantitative PCR analysis

RNA was extracted from cells using the RNeasy Plus Mini Kit (Qiagen) according to the manufacturer's protocol. For gene expression analysis, cDNA was generated from 1 μg RNA with the iScript cDNA synthesis kit (Bio-Rad) as per the manufacturer's protocol. Using the QuantiTect SYBR Green PCR kit, 100 ng of cDNA was amplified according to the manufacturer's instructions with primers targeting *BUB1B* (catalogue no. QT00008701), *MAD2* (catalogue no. QT00094955), *TTK* (catalogue no. QT00035168), *KIF18A* (catalogue no. QT00042455), or *GAPDH* (catalogue no. QT00273322) as an endogenous control (QuantiTect Primer Assay, Qiagen). Data analysis was performed with QuantStudio 6 and 7 Flex Real-Time PCR System Software v1.0 (Applied Biosystems, Life Technologies) using the $\Delta\Delta Ct$ method.

Western blotting

Processed total cell lysates were separated by SDS–PAGE. Protein size was estimated using 'PrecisionPlus All Blue' or 'PrecisionPlus Kaleidoscope' protein markers (BioRad). Separated proteins were then transferred to a methanol-activated polyvinylidene difluoride membrane (PVDF, Roche) using wet transfer Mini-PROTEAN II electrophoresis (BioRad), or to nitrocellulose membrane (BioRad) using Trans-Blot Turbo electrophoresis system (BioRad). Membranes were blocked in 5% skim milk (Fluka) in Tris-buffered saline with 0.05% Tween20 (TBST), decorated with the respective primary antibodies diluted in blocking solution overnight at 4 °C with gentle agitation. Further, the membranes were rinsed for 30 min with TBST with a triple buffer exchange, incubated with HRP-conjugated secondary antibodies (R&D Systems), followed by triple TBST wash, chemiluminescence using ECLplus kit and detection either on ECL hyperfilm (GE Healthcare), on X-ray hyperfilm processor MI-5 (Medical Index) or using Fujifilm Luminescent Image Analyzer (LAS-3000 Lite) system (Fujifilm). Protein band quantification was carried out using ImageJ (National Institutes of Health, http://rsb.info.nih.gov/ij/). The following primary antibodies were used: anti-KIF18A rabbit[62] (1:500), affinity-purified polyclonal antibody raised against an N-terminal GST-tagged fragment (KIF18^{AbN}), a gift from Dr Thomas Mayer, University of Konstanz, Germany; anti-KIF18A rabbit (1:5,000), Bethyl Laboratories (catalogue no. A301-080A); anti-GAPDH goat (1:1,000), Abcam (catalogue no. ab9483); anti-α-Tubulin mouse (1:2,000), Sigma (catalogue no. T6199). Uncropped scans of all gels are shown in Supplementary Fig. 4.

Transcriptional profiling

Cells were exposed to reversine (250 nM or 500 nM) or to MPI-0479605 (250 nM) and transcriptional profiling was performed 6 h, 24 h and 72 h after drug exposure. DMSO was used as a negative control, and 1 μM mitoxantrone or 10 μM reversine were used as positive cytotoxic controls. The L1000 expression-profiling assay was performed as previously described[63,64]. First, mRNA was captured from cell lysate using oligo dT-coated 384-well Magnefy microspheres. The lysate was then

removed, and a reverse-transcription mix containing Superscript IV reverse transcriptase was added. The plate was washed and a mixture containing both upstream and downstream probes for each gene was added. Each probe contained a gene-specific sequence, along with a universal primer site. The upstream probe also contained a microbead-specific barcode sequence. The probes were annealed to the cDNA over a 6-h period, and then ligated together to form a PCR template. After ligation, Platinum *Taq* and universal primers were added to the plate. The upstream primer was biotinylated to allow later staining with streptavidin–phycoerythrin. The PCR amplicon was then hybridized to Luminex microbeads via the complimentary, probe-specific barcode on each bead. After overnight hybridization, the beads were washed and stained with streptavidin–phycoerythrin to prepare them for detection in Luminex FlexMap 3D scanners. The scanners measured each bead independently and reported the bead colour and identity and the fluorescence intensity of the stain. A deconvolution algorithm converted these raw fluorescence intensity measurements into median fluorescence intensities for each of the 978 measured genes, producing the GEX level data. These GEX data were normalized using an invariant gene set, and then quantile-normalized to produce QNORM level data. An inference model was applied to the QNORM data to infer gene expression levels for a total of 10,174 features (Supplementary Table 7). Per-strain gene expression signatures were calculated using a weighted average of the replicates, for which the weights are proportional to the Spearman correlation between the replicates. These signatures were then queried against the reference data set Touchstone (GEO accession no. GSE92742)[63] to assess similarity. The top 100 up- and downregulated genes in each signature were compared to the reference data, yielding a rank-ordered list of most similar reference signatures.

For downstream analyses (unsupervised clustering and GSEA), differential gene expression profiles were computed for the L1000 profiles. In order to maximize the expression signal, differential expression was computed jointly using profiles measured at 24 h and 72 h for each cell line and drug treatment. Specifically, log-fold-change was estimated between drug-treated profiles at 24 and 72 h and DMSO-treated profiles at 24 and 72 h for each experimental condition. This estimation was carried out using the 'limma-trend' pipeline[54], in which *P* values were estimated on the basis of empirical Bayes-moderated *t*-statistics. Unsupervised hierarchical clustering was performed on these differential expression profiles using complete-linkage clustering, as implemented in the R function 'hclust'. Pearson correlation was used as a similarity measure between the expression profiles. For analysis of gene set enrichment of transcriptional response signatures, enrichment was measured using the original GSEA method[65] (based on the estimated log fold-change), which estimates the concentration of each gene set in the list of up- and downregulated genes. We used the GSEA implementation in the R package 'fgsea'[66]. The collection of gene sets used was the 'Biological Processes' gene set collection from MSigDB v6.2[67].

The analysis of the mRNA expression levels of mitotic kinesins was based on microarray-based transcriptional profiling of HCT116 and HPT cells (GEO accession no. GSE47830)[68].

Microscopy
Cells were grown on plain glass, FBN-coated or gelatin-coated coverslips. For analysis, cells were either fixed in cold methanol followed by 4% paraformaldehyde, blocked with 10% FBS in PBS-T, or cold methanol containing 1% paraformaldehyde, blocked with 20% goat serum in antibody-diluting buffer (Abdil; TBS, pH 7.4, 1% BSA, 0.1% Triton X-100, and 0.1% sodium azide) before incubating with the specified primary antibodies. Coverslips were mounted onto slides using Prolong Gold anti-fade mounting medium with DAPI (Molecular Probes). Images were acquired with a microscope (Axio Imager Z1; Carl Zeiss) equipped with a CSU22 unit (Yokogawa Corporation of America) and CoolSnap HQ2 camera (Photometrics) controlled by SlideBook software or a

Ti-E inverted microscope (Nikon Instruments) with a Clara cooled charge-coupled device (CCD) camera, Spectra-X light engine (Lumencore) (Andor) controlled by NIS Elements software (Nikon Instruments). Imaging of *z*-stacks with 0.3–0.7-μm steps covering the entire volume of the mitotic apparatus were collected with a Plan-Apochromatic 1.40 NA 60× or 100× immersion oil objective lens. Live-cell imaging of cells in CO_2-independent medium (Gibco) used Nikon Plan Apo 20× or 40× DIC N2 0.75 NA objectives and an environmental chamber at 37 °C.

Mitotic arrest assay
Cells were seeded in black 96-well plates two days before imaging and treated with Nocodazole at a concentration of 200 ng/ml. Imaging was performed with a 6-min time-lapse for 50 h with GFP (1,000 ms exposure) and DIC (200 ms exposure) using a 20× air objective. Image analysis was performed using Slidebook 6 software (Intelligent Imaging Innovations).

Microtubule regrowth assay
The microtubule regrowth assay was performed as previously described[69]. The cells were incubated with 1 μg ml^{-1} nocodazole for 3 h and placed in ice for 1 h to depolymerize microtubules. Microtubule regrowth was analysed after transfer to drug-free medium at 37 °C. Cells were washed in PHEM buffer and depolymerized tubulin was removed with 0.2% Triton in PHEM buffer for 1 min. The cells were then washed in 1× PBS and fixed in 3.7% formaldehyde for 15 min. An immunofluorescence assay for β-tubulin and pericentrin was performed after permeabilization in 0.5% Triton and blocking in PBTA. Quantification of mean β-tubulin fluorescence intensity in the region of the centrosome was measured using ImageJ in a circle of constant diameter across all samples around the centrosome. At least 40 cells were analysed in each sample of three independent biological experiments.

Microtubule dynamics by EB3 tracking
Cells transfected with EB3–EGFP were seeded in 96-well glass bottom plate. Twenty-four hours later, the VS83 was added for 18 h. Spinning disk confocal microscope with an incubator box was used for the microscopy. Live cell 60-s movies were taken using a spinning disk confocal microscope with a 100× objective, *z*-stacks 400 nm, time resolution 400 ms. The mean velocity was calculated as the instantaneous velocity between at least three consecutive times as $v =$ mean distance (μm)/time (s).

Quantitative analysis of spindle angle and length
Images were collected by taking *z*-stacks with a step size of 0.3 μm covering the entire volume of the mitotic spindle. Fluorescence signal quantification in the spindle was performed using the SlideBook software. Distances were measured after defining the position of the two poles and correcting for projection errors.

Quantification of multipolar spindles, micronuclei and unsuccessful cytokinesis
Multipolar spindles and micronuclei were counted in cells labelled with antibodies against α-tubulin and γ-tubulin, as well as DAPI. The percentage of mitotic cells with spindles containing more than two poles and the percentage of interphase cells with micronuclei are reported. The percentage of cells that exited mitosis as a single cell was determined from live imaging of cells using DIC and reported as those that fail cytokinesis.

Karyotyping
Low-pass whole-genome sequencing (LP-WGS). Genomic DNA was extracted using a Qiagen extraction kit (Qiagen), amplified and barcoded using Nextera reagents (Illumina). Whole-genome-amplified DNA samples were purified with 1.5× SPRI beads in an automated setup. Post purification, Illumina libraries were made using the Illumina Nextera

XT kit. Samples were pooled, quantified by qPCR, and sequenced on HiSeq2000 on Single End flowcell lanes. Sequence reads were trimmed to 40 nucleotides and aligned to the mouse (mm9) or human (hg19) reference genomes using the BWA (0.7.12) backtrack algorithm. HMMcopy (0.1.1)[70] was used to detect copy number alterations by estimating DNA copy number in 500-kb bins controlling for mappability and GC content (calculated by HMMcopy gcCounter). CNV analyses were performed as described[71], running HMMcopy with e value = 0.995, and a dnacopy (1.50.1) run with alpha = 0.0001.

G-banding. The cells were treated with 50 ng/ml of the microtubule-depolymerizing drug colchicine (Serva) for 4.5 h, then centrifuged with a table-top centrifuge, swollen in 75 mM KCl in a 37 °C water bath for 15 min, fixed with Carnoy solution (75% methanol and 25% acetic acid) and spread on a wet glass slide with a glass Pasteur pipette. The slides were dried at 42 °C and stained with Giemsa dye (Fluka). The slides were imaged with an inverted microscope with a 100× objective; 30–50 metaphases were scored for each cell line.

Single-cell DNA sequencing

For single-nucleus isolation, cell pellets were re-suspended in lysis buffer (1 M tris-HCl pH 7.4, 5 M NaCl, 1 M CaCl₂, 1 M MgCl₂, 7.5% BSA, 10% NP-40, ultra-pure water, 10 mg/ml Hoechst 33358, 2 mg/ml propidium iodide (PI)) and kept on ice in the dark for 15 min to facilitate lysis. G1 single nuclei, as assessed by propidium iodide and Hoechst staining, were sorted into 96-well plates on a BD FacsJAZZ cell sorter (BD Biosciences), and stored at −80 °C until further analysis. For single-cell library preparation, single nuclei were lysed and DNA was barcoded, followed by automated library preparation (Bravo Automated Liquid Handling Platform, Agilent Technologies), as previously described[72]. Pooled single-cell libraries were sequenced using a NextSeq 500 machine (Illumina; up to 77 cycles; single-end). The generated data were subsequently demultiplexed using sample-specific barcodes and changed into fastq files using bcl2fastq (Illumina; version 1.8.4). Reads were aligned to the human reference genome (GRCh38/hg38) using Bowtie2 (version 2.2.4)[73]. Duplicate reads were marked with BamUtil (version 1.0.3)[74]. The aligned read data (bam files) were analysed with AneuFinder (Version 1.14.0)[41,75]. Following GC correction and blacklisting of artefact-prone regions (extreme low or high coverage in control samples), libraries were analysed using the dnacopy and edivisive copy number calling algorithms with variable width bins (binsize: 1 Mb; stepsize: 500 kb) and breakpoint refinement (R = 20, confint = 0.95; other settings as default). A minimum concordance of 95% between the results of the two algorithms was required. Libraries with less than five reads per bin per chromosome copy (~30,000 reads for a diploid genome) were discarded. Samples with a near-tetraploid DNA content were analysed with the developer version of AneuFinder (Version 1.7.4; from GitHub): the min.ground.ploidy parameter was set to either 3 or 3.5 and the max.ground.ploidy parameter to 4.5, 5.0 or 5.5. The minimum and maximum ground ploidy values were determined with the results that were previously obtained with the standard (Bioconductor) version of AneuFinder. Results were subsequently curated as described above, except using a minimum concordance of 90%. Aneuploidy and heterogeneity scores were calculated as previously described[41]. Overall, high-quality karyotypes were generated for 210 single cells.

Flow cytometry

For cell cycle and cell death analyses, cells were trypsinized and incubated in cold PBS supplemented with 5% fetal calf serum (Sigma-Aldrich; PBS-FACS). DNA was stained with either PI or Hoechst. For PI staining, cold 70% ethanol was added to the cells dropwise, followed by 30 min incubation on ice. The fixed cells were centrifuged and pellets were washed twice with PBS-FACS. We added 50 µl RNase A solution (100 µg/ml in PBS) to the pellet, followed by staining with 400 µl PI solution (50 µg/ml in PBS) per million cells. Cells were incubated for 10 min at 25 °C.

For Hoechst staining, pellets were incubated in the dark with 10 mg/ml Hoechst 33358 for 15 min at 4 °C. Data acquisition was performed using the CytoFLEX flow cytometer (Beckman Coulter) or the BD FacsJAZZ cell sorter (BD Biosciences). Data analysis was performed using Kaluza Analysis software 2.1 (Beckman Coulter).

Gating strategy

An SSC-A/FSC-A gate was set in order to exclude cell debris, and an FSC-A/FSC-H gate was then set in order to exclude doublets. Cell cycle phases were determined manually using linear gating based on the 2N and 4N peaks of the histogram. Cell death was assessed by quantifying the fraction of cells in the sub-G1 population, and mitotic arrest was assessed by quantifying the fraction of cells in the G2/M population. Gating strategy is shown in Supplementary Fig. 3.

Statistical analyses

The two-sided t-test was used to compare single gene dependency and expression between the near-euploid and highly aneuploid cancer cell lines. The two-sided Fisher's exact test was used for calculating the significance of the overlap of hits for the genetic perturbation data sets. The statistical analyses of all microscopy experiments were performed in GraphPad Prism. t-test was used to determine the significance of differences between the means of two groups. Fisher's exact test was used to determine the significance of differences in the prevalence of categorical events between groups.

Reporting summary

Further information on research design is available in the Nature Research Reporting Summary linked to this paper.

Code availability

The code used to generate and/or analyse the data are publicly available, or available upon request.

Data availability

All datasets are available within the article and its Supplementary Information, or from the Corresponding Author upon request. Cell line aneuploidy profiles and scores are available at the DepMap portal (https://depmap.org/portal/). The analysed CCLE genomic data are available at https://doi.org/10.6084/m9.figshare.11384241.v2. LP-WGS data have been deposited to SRA with BioProject accession number PRJNA672256.

48. McFarland, J. M. et al. Improved estimation of cancer dependencies from large-scale RNAi screens using model-based normalization and data integration. *Nat. Commun*. **9**, 4610 (2018).
49. Seashore-Ludlow, B. et al. Harnessing connectivity in a large-scale small-molecule sensitivity dataset. *Cancer Discov*. **5**, 1210–1223 (2015).
50. Rees, M. G. et al. Correlating chemical sensitivity and basal gene expression reveals mechanism of action. *Nat. Chem. Biol*. **12**, 109–116 (2016).
51. Iorio, F. et al. A landscape of pharmacogenomic interactions in cancer. *Cell* **166**, 740–754 (2016).
52. Nusinow, D. P. et al. Quantitative proteomics of the cancer cell line encyclopedia. *Cell* **180**, 387–402.e16 (2020).
53. Chan, E. M. et al. WRN helicase is a synthetic lethal target in microsatellite unstable cancers. *Nature* **568**, 551–556 (2019).
54. Ritchie, M. E. et al. limma powers differential expression analyses for RNA-sequencing and microarray studies. *Nucleic Acids Res*. **43**, e47 (2015).
55. Benjamini, Y. & Hochberg, Y. Controlling the false discovery rate: a practical and powerful approach to multiple testing. *J. R. Stat. Soc. B* **57**, 289–300 (1995).
56. Sheltzer, J. M. A transcriptional and metabolic signature of primary aneuploidy is present in chromosomally unstable cancer cells and informs clinical prognosis. *Cancer Res*. **73**, 6401–6412 (2013).
57. Pedregosa, F. et al. Scikit-learn: machine learning in Python. *J. Mach. Learn. Res*. **12**, 2825–2830 (2011).
58. R core team. *R: A Language and Environment for Statistical Computing* (R Foundation for Statistical Computing, 2018).
59. Huang, D. W. et al. DAVID Bioinformatics Resources: expanded annotation database and novel algorithms to better extract biology from large gene lists. *Nucleic Acids Res*. **35**, W169–W175 (2007).

60. Dempster, J. M. et al. Extracting biological insights from the Project Achilles Genome-Scale CRISPR Screens in cancer cell lines. Preprint at https://doi.org/10.1101/720243 (2019).

61. Berg, S. et al. ilastik: interactive machine learning for (bio)image analysis. *Nat. Methods* **16**, 1226–1232 (2019).

62. Mayr, M. I. et al. The human kinesin Kif18A is a motile microtubule depolymerase essential for chromosome congression. *Curr. Biol.* **17**, 488–498 (2007).

63. Subramanian, A. et al. A next generation connectivity map: L1000 platform and the first 1,000,000 profiles. *Cell* **171**, 1437–1452.e17 (2017).

64. Ben-David, U. et al. Genetic and transcriptional evolution alters cancer cell line drug response. *Nature* **560**, 325–330 (2018).

65. Subramanian, A. et al. Gene set enrichment analysis: a knowledge-based approach for interpreting genome-wide expression profiles. *Proc. Natl Acad. Sci. USA* **102**, 15545–15550 (2005).

66. Korotkevich, G. et al. Fast gene set enrichment analysis. Preprint at https://doi.org/10.1101/060012 (2016).

67. Liberzon, A. et al. Molecular signatures database (MSigDB) 3.0. *Bioinformatics* **27**, 1739–1740 (2011).

68. Dürrbaum, M. et al. Unique features of the transcriptional response to model aneuploidy in human cells. *BMC Genomics* **15**, 139 (2014).

69. Lee, K. & Rhee, K. PLK1 phosphorylation of pericentrin initiates centrosome maturation at the onset of mitosis. *J. Cell Biol.* **195**, 1093–1101 (2011).

70. Lai, D. & Shah, S. HMMcopy: copy number prediction with correction for GC and mappability bias for HTS data. https://rdrr.io/bioc/HMMcopy/ (2012).

71. Knouse, K. A., Wu, J. & Amon, A. Assessment of megabase-scale somatic copy number variation using single-cell sequencing. *Genome Res.* **26**, 376–384 (2016).

72. van den Bos, H. et al. in *Cellular Senescence. Methods in Molecular Biology* (ed. Demaria, M.) (Humana, 2019).

73. Langmead, B. & Salzberg, S. L. Fast gapped-read alignment with Bowtie 2. *Nat. Methods* **9**, 357–359 (2012).

74. Jun, G., Wing, M. K., Abecasis, G. R. & Kang, H. M. An efficient and scalable analysis framework for variant extraction and refinement from population-scale DNA sequence data. *Genome Res.* **25**, 918–925 (2015).

75. van den Bos, H. et al. Single-cell whole genome sequencing reveals no evidence for common aneuploidy in normal and Alzheimer's disease neurons. *Genome Biol.* **17**, 116 (2016).

Author contributions U.B.-D. conceived the project. Y.C.-S., M.A., H.T. and U.B.-D. performed the cell culture experiments. K.L and J.Z. assisted with cell culture experiments. C.M., H.L.H.M. and J.S. performed microscopy experiments. Z.S. provided the HCT116/HPT and RPE1/RPT cell lines, and together with S.V.B. and L.-M.S. characterized them and performed microscopy experiments. S.S. provided aneuploid RPE1 cell lines, and together with M.R.I. characterized them and examined their sensitivity to SAC inhibition. I.B., R.W., D.C.J.S. and F.F. generated, processed and assisted in the analysis of the single-cell DNA sequencing data. J.M.M., M.K. and U.B.-D. performed the computational analyses. N.L. assisted with the generation of the gene expression data, and A.J. assisted with their analysis. A.N. and A.J.B. shared data. F.F., R.B., S.S. T.R.G., J.S., Z.S. and U.B.-D. supervised the experiments and analyses that were conducted in their respective laboratories. U.B.-D. directed the project and wrote the manuscript with input from all co-authors.
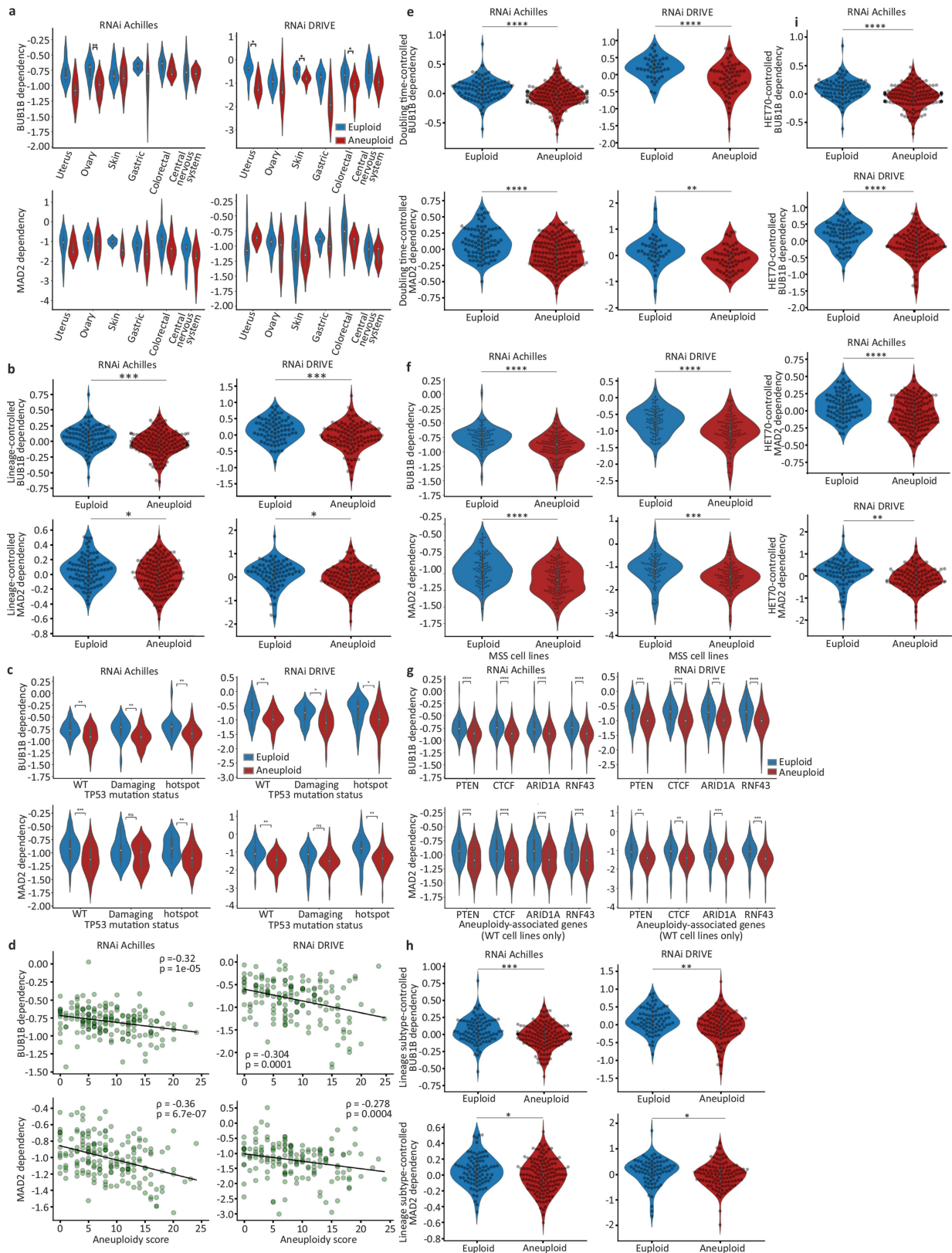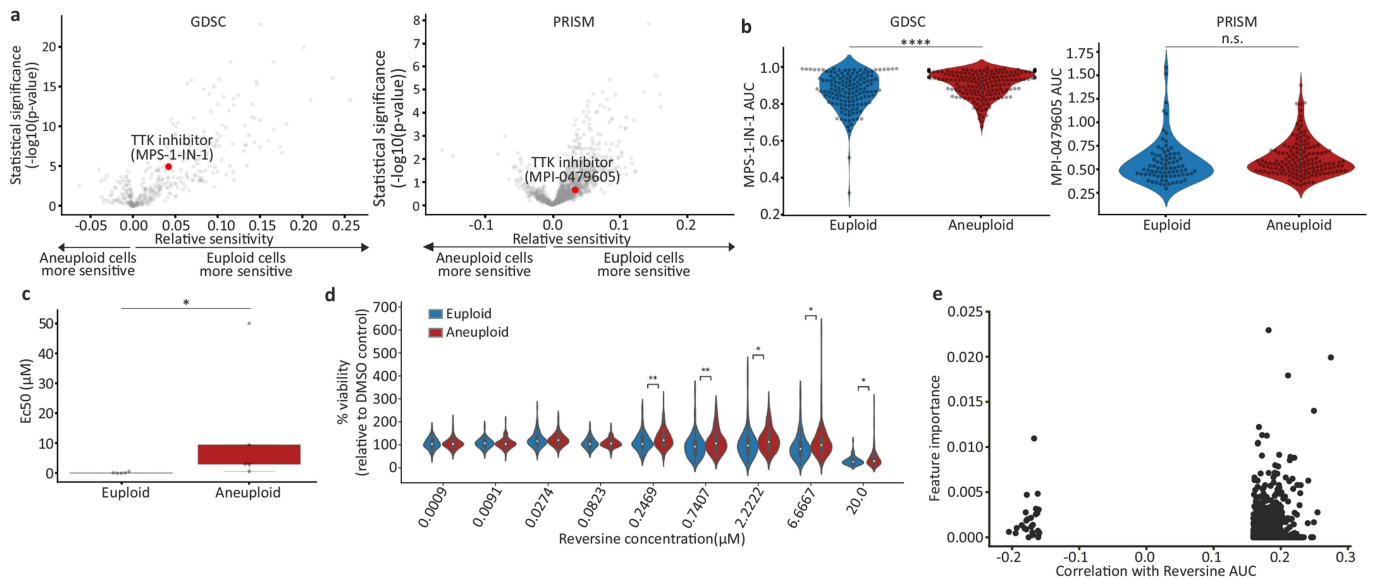
Extended Data Fig. 1 | See next page for caption.

Extended Data Fig. 1 | Increased sensitivity of aneuploid cancer cells to genetic inhibition of the spindle assembly checkpoint. a, Copy number profiles of 5 representative breast cancer cell lines from the highly-aneuploid cell line group (top quartile of AS) and 5 representative breast cancer cell lines from the near-euploid cell line group (bottom quartile of AS). **b**, A volcano plot showing the differential genetic dependencies between the near-euploid and highly-aneuploid cancer cell lines (top vs. bottom quartiles), based on the genome-wide DRIVE RNAi screen[4]. BUB1B and MAD2, core members of the SAC, are highlighted in red. **c**, A Venn diagram showing the overlap of the differentially-dependent genes (q<0.25) between the Achilles and DRIVE RNAi screens. ****P=1e-16, two-tailed Fisher's exact test. **d**, The pathways enriched in the list of genes that are more essential in near-euploid than in highly-aneuploid cancer cell lines (effect size <-0.1, q < 0.1) in the DRIVE RNAi screen, based on DAVID functional annotation enrichment analysis[59]. The full list is available in Supplementary Table 3. *, Benjamini-corrected p-value <0.1; one-tailed Fisher's Exact Test. **e**, The sensitivity of near-euploid and highly-aneuploid cancer cell lines to the knockdown of *BUB1B* (left) and *MAD2* (right) in the DRIVE RNAi screen. The more negative a value, the more essential the gene is in that cell line. ****P=2e-06 and P=1e-04 for *BUB1B* and *MAD2*, respectively; two-tailed t-test. **f**, A volcano plot showing the differential genetic dependencies between the near-euploid and highly-aneuploid cancer cell lines (top vs. bottom 10% of cell lines), based on the genome-wide DRIVE RNAi screen[4]. *BUB1B*, *MAD2* and *KIF18A* are highlighted in red. **g**, The sensitivity of near-euploid and highly-aneuploid cancer cell lines to the knockdown of *BUB1B* (left) and *MAD2* (right) in the DRIVE RNAi screen (top vs. bottom 10% of cell lines). The more negative a value, the more essential the gene is in that cell line. *P=0.037; ***P=5e-04; two-tailed t-test. **h**, Comparison of protein expression levels of BUB1B (left) and MAD2 (right) between near-euploid and highly-aneuploid cancer cell lines. n.s., P>0.05; **P=0.001; for BUB1B and MAD2, respectively; two-tailed t-test. **i**, The correlations between the mRNA expression levels of *BUB1B* (top) and *MAD2* (bottom) and the genetic dependency on these genes in the Achilles (left) and DRIVE (right) RNAi screens. Spearman's ρ = 0.36 (P=3e-08), 0.31 (P=2e-06), 0.26 (P=4e-04) and 0.40 (P=2e-08), respectively. **j**, The correlations between the protein expression levels of BUB1B (top) and MAD2 (bottom) and the genetic dependency on these genes in the Achilles (left) and DRIVE (right) RNAi screens. Spearman's ρ = 0.11 (P=0.09), 0.26 (P=4e-05), 0.14 (P=0.016) and 0.24 (P=5e-05), respectively. **k**, The mRNA expression levels of *BUB1B* (left) and *MAD2* (right) in near-euploid and highly-aneuploid cancer cell lines across multiple cell lineages. *P<0.05; two-tailed t-test.
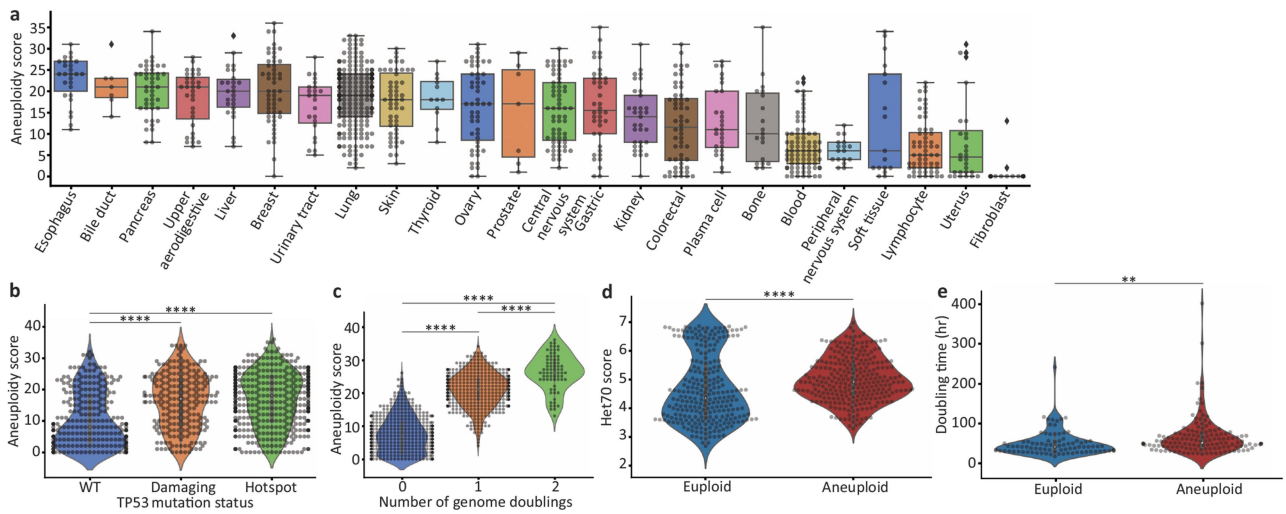
Extended Data Fig. 2 | Genomic and phenotypic features associated with the degree of aneuploidy in human cancer cell lines. a, The AS distribution across 23 cancer types. Bar, median; box, 25th and 75th percentile; whiskers, 1.5 X IQR, individual cell lines. **b**, Comparison of AS between cancer cell lines with distinct *TP53* mutation status (based on CCLE annotations)[2]. **** P = 6e-15 and P = 1e-22 for the comparisons between *TP53*-WT and 'damaging' and *TP53*-WT and 'hotspot' mutations, respectively; two-tailed *t*-test. **c**, Comparison of AS between cancer cell lines with distinct genome doubling (WGD) status.

**** P = 1e-192, P = 2e-96 and P = 6e-13 for the comparisons between WGD = 0 and WGD = 1, WGD = 0 and WGD = 2, and WGD = 1 and WGD = 2, respectively; two-tailed *t*-test. **d**, Comparison of the HET70 score, a measure of karyotypic instability[56], between the near-diploid and highly-aneuploid cell line groups. **** P = 2e-08; two-tailed *t*-test. **e**, Comparison of doubling time between the near-diploid and highly-aneuploid cell line groups. ** P = 0.005; two-tailed *t*-test.

**Extended Data Fig. 3** | See next page for caption.

Article

Extended Data Fig. 4 | Reduced sensitivity of aneuploid cancer cells to chemical inhibition of the spindle assembly checkpoint. a, Volcano plots showing the differential drug sensitivities between the near-euploid and highly-aneuploid cancer cell lines, based on the large-scale GDSC[6] and PRISM screens[9]. MPS1IN-1 and MPI-0479605, the only SAC inhibitors included in each screen, respectively, are highlighted in red. **b**, The sensitivity of near-euploid and highly-aneuploid cancer cell lines to the SAC inhibitors MPS1-IN-1 and MPI-0479605 in the GDSC (left) and PRISM (right) screens. ****P = 1e-0.5; n.s., P = 0.23; two-tailed t-test. **c**, Experimental validation of the response of 5 near-euploid (CAL51, EN, MHHNB11, SW48 and VMCUB1) and 5 highly-aneuploid (MDAMB468, NCIH1693, PANC0813, SH10TC and A101D) cell lines to

72h exposure to the SAC inhibitor reversine. *P = 0.016, two-tailed Wilcoxon rank-sum test; n = 5 cell lines in each group. Bar, median; box, 25th and 75th percentile; whiskers, 1.5 X IQR. **d**, Comparison of the sensitivity to reversine between near-euploid and highly-aneuploid cancer cell lines subjected to the PRISM cell viability assay, confirming the reduced sensitivity of highly-aneuploid cells to a 120h exposure to SAC inhibitors. n.s., P > 0.05; *P < 0.05; **P < 0.01; two-tailed t-test. **e**, An association analysis failed to identify a genomic biomarker of reversine sensitivity. Shown are the top 1000 genomic features identified by our model (see Methods). No feature stands out in terms of importance and/or correlation, and the overall predictive value is poor.
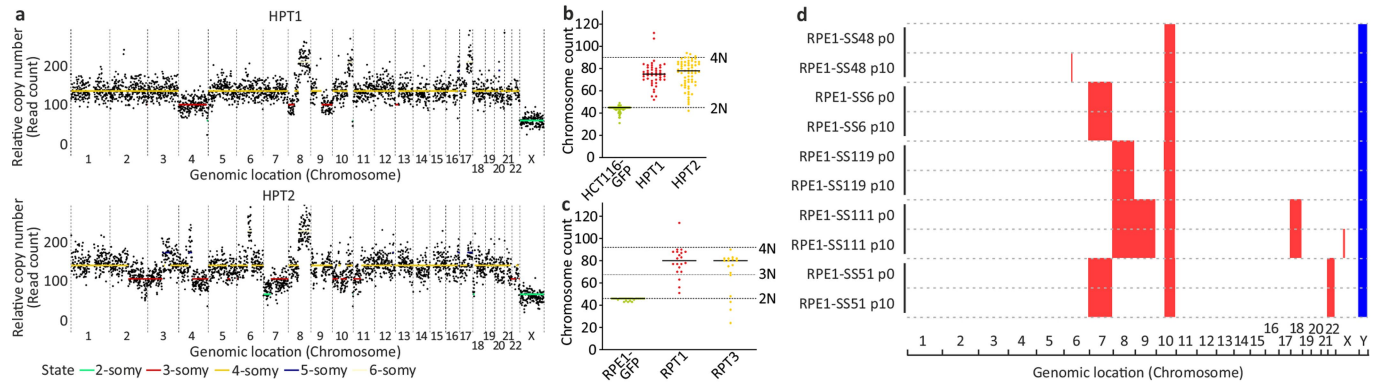
Extended Data Fig. 5 | Isogenic model systems of near-diploid and aneuploid cell lines. a, scDNaseq-based copy number profiling of the HPT1 and HPT2 aneuploid cell lines. **b**, Karyotyping-based chromosome count of the near-diploid HCT116 cells and their highly-aneuploid HPT derivatives. Each dot represents a metaphase spread. Average chromosome number: $n = 45$, $n = 75$ and $n = 78$, for HCT116-GFP, HPT1 and HPT2, respectively. **c**, Karyotyping-based chromosome count of the near-diploid RPE1 cells and their highly-aneuploid RPT derivatives. Each dot represents a metaphase spread. Average chromosome number: $n = 46$, $n = 80$ and $n = 76.5$, for RPE1-GFP, RPT1 and RPT2, respectively. **d**, Low-pass whole-genome sequencing-based karyotyping of near-diploid and aneuploid RPE1 clones. No karyotypic changes have been observed between passage 0 (p0) and passage 10 (p10) of each clone. Red, large (>5Mb) gains (log2CN >0.3); blue, large (>5Mb) losses (log2CN <-0.3).
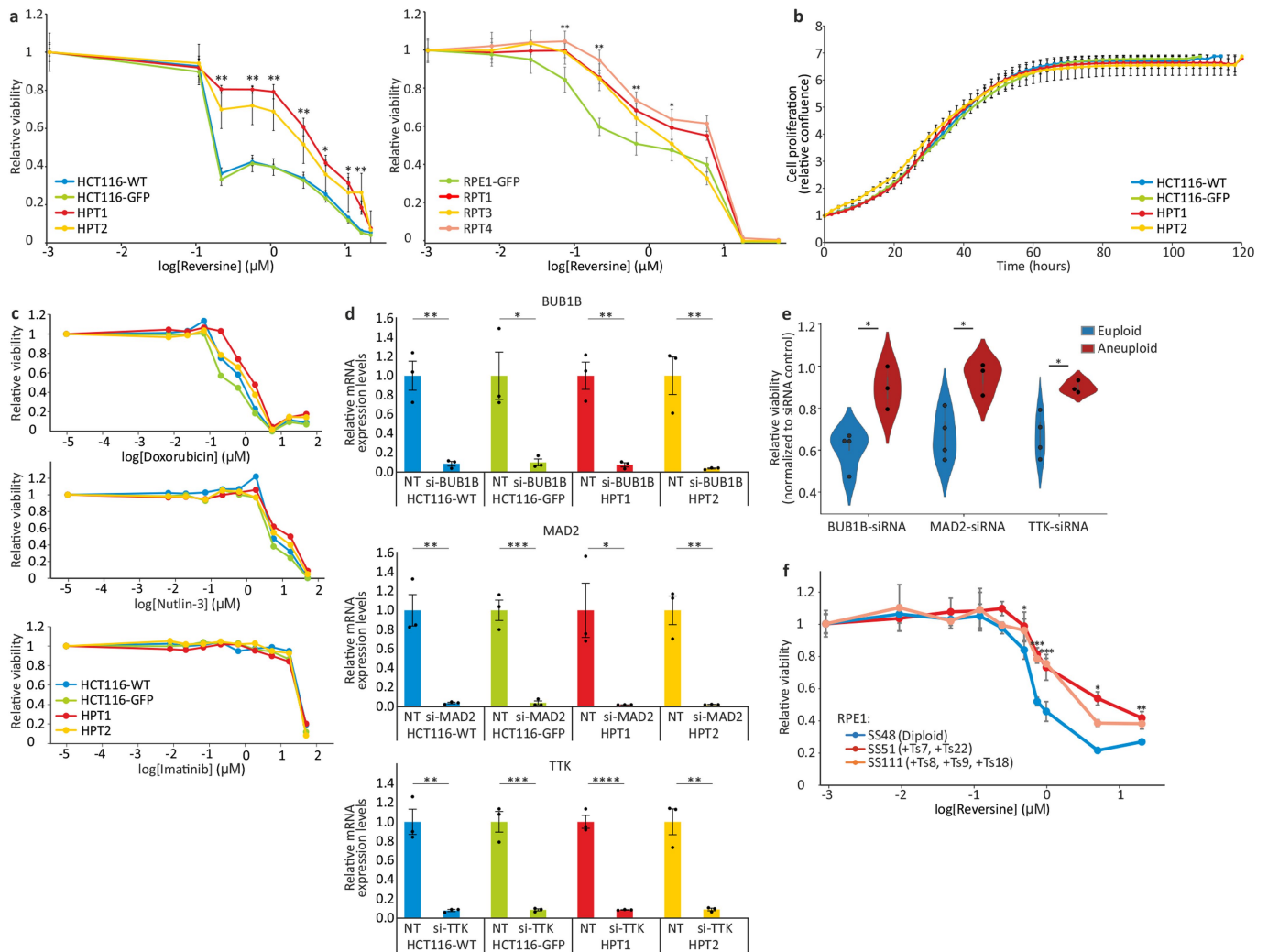
Extended Data Fig. 6 | The effect of aneuploidy on cellular sensitivity to SACi in isogenic human cell lines. a, Left: dose response curves of the response of near-diploid HCT116 cells and their highly-aneuploid derivatives HPT cells, to the SAC inhibitor reversine following 120h of drug exposure. $EC_{50} = 0.11\mu M$, $0.11\mu M$, $2.32\mu M$ and $1.06\mu M$, for HCT116-WT, HCT116-GFP, HPT1 and HPT2, respectively. Right: dose response curves of the response of near-diploid RPE1 cells and their highly-aneuploid derivatives RPT cells, to the SAC inhibitor reversine following 120h of drug exposure. $EC_{50} = 0.13\mu M$, $1.82\mu M$, $0.57\mu M$ and $2.07\mu M$, for RPE1-GFP, RPT1, RPT3 and RPT4, respectively. $*P < 0.05$; $**P < 0.01$; $***P < 0.001$; two-tailed t-test. Data represent the mean ± s.d.; $n = 3$ biological replicates. **b**, Time-lapse imaging-based proliferation curves of HCT116 and HPT cells under standard culture conditions. Data represent the mean ± s.d.; $n = 3$ biological replicates. **c**, Dose response curves of the response of HCT116 and HPT cells to three drugs with unrelated mechanisms of action. Doxorubicin $EC_{50} = 0.61\mu M$, $0.32\mu M$, $1.2\mu M$ and $0.89\mu M$; Nutlin-3 $EC_{50} = 11.88\mu M$, $19.28\mu M$, $15.26\mu M$ and $65.11\mu M$; Imatinib $EC_{50} = 17.94\mu M$, $19.08\mu M$, $18.77\mu M$ and $23.31\mu M$; for HCT116-WT, HCT116-GFP, HPT1 and HPT2, respectively. **d**, Relative mRNA expression levels of *BUB1B*,

MAD2 and *TTK*, confirming successful siRNA-mediated knockdown of each gene in all cell lines. $*P = 0.011$, $P = 0.012$ for HCT116-GFP and HPT1, respectively; $**P = 0.0019$, $P = 0.0015$, $P = 0.0039$ for BUB1B in HCT116-WT, HPT1 and HPT2, respectively; $P = 0.0021$, $P = 0.0013$ for MAD2 in HCT116-WT and HPT2, respectively; $P = 0.0011$, $P = 0.0012$ for TTK in HCT116-WT and HPT2, respectively; $***P = 0004$, $P = 0.0005$ for MAD2 and TTK in HCT116-GFP, respectively; $****P = 9e\text{-}05$; one-tailed t-test; $n = 3$ biological replicates. Data represent the mean ± s.e.m. **e**, The relative viability of 4 near-diploid (CAL51, EN, MHHNB11, VMCUB1) and 3 highly-aneuploid (MDAMB468, PANC0813, SH0TA) cancer cell lines following 72h of siRNA-mediated knockdown of 3 SAC components: BUB1B, MAD2 and TTK. Results are normalized to a non-targeting siRNA control. $*P = 0.010$, $P = 0.016$, and $P = 0.015$, for BUB1B, MAD2 and TTK, respectively; two-tailed t-test. Error bars, s.d. **f**, Dose response curves of the response of the near-diploid RPE1 clone SS48 and its isogenic aneuploid clones SS51 (+Ts7, +Ts22) and SS111 (+Ts8, +Ts9, +Ts18), to the SAC inhibitor reversine following 120h of drug exposure. $EC_{50} = 0.66\mu M$, $1.03\mu M$ and $1.03\mu M$, for SS48, SS51 and SS111, respectively $*P < 0.05$; $**P < 0.01$; $***P < 0.001$; two-tailed t-test. Data represent the mean ± s.d.; $n = 3$ biological replicates.
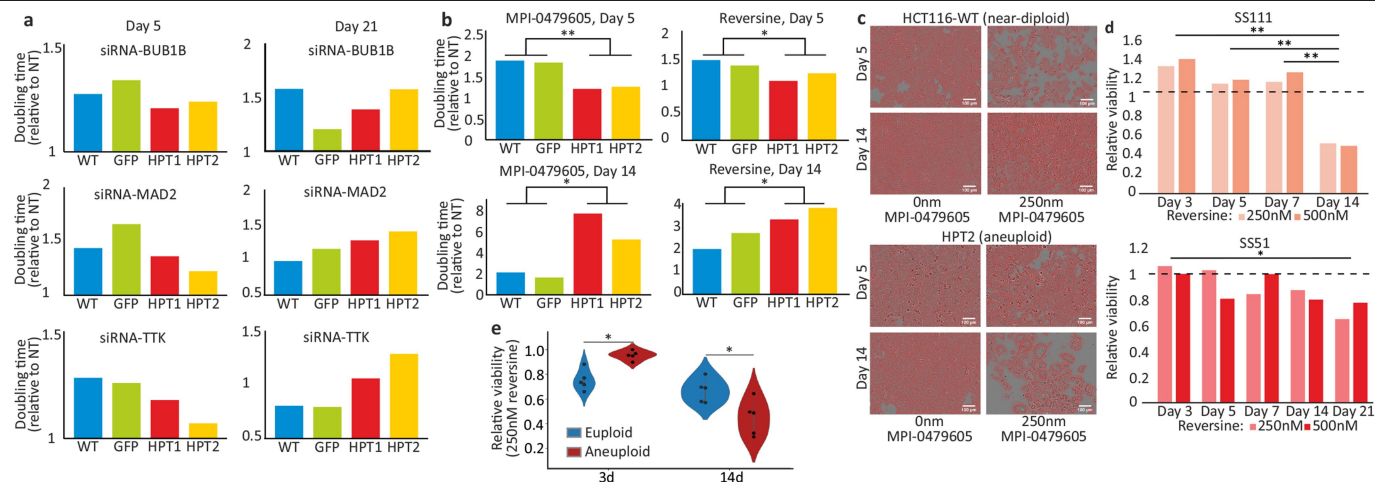
Extended Data Fig. 7 | Time-dependent increased sensitivity of aneuploid cancer cells to genetic and chemical SACi. a, Comparison of the doubling times of HCT116 and HPT cells exposed to siRNAs against BUB1B, MAD2 or TTK. The drug effect of SACi is stronger in the near-diploid HCT116 cells at d5, but is stronger in the highly-aneuploid HPT cells at d21. **b**, Comparison of the doubling times of HCT116 and HPT cells exposed to the SAC inhibitors MPI-0479605 or reversine. The drug effect of SACi is stronger in the near-diploid HCT116 cells at d5, but at d21 it becomes stronger in the highly-aneuploid HPT cells. *$P = 0.034$, $P = 0.046$ and $P = 0.049$ for MPI-0479605 and reversine at d5 and d14, respectively; **$P = 0.0015$; one-tailed t-test; $n = 2$ independent cell lines. **c**, Representative images of cells from the drug experiment (same images as in Fig. 2g), with cell masking performed using the image analysis software

ilastik[61]. Scale bar, 100 μm. **d**, The relative viability of the aneuploid RPE1 clones, SS111 and SS51, following reversine exposure. The viability effect was normalized to the effect of the drug in the near-diploid RPE1 clone, SS48. The drug effect of SACi is comparable during the first week of drug exposure, but the highly-aneuploid cells become significantly more sensitive with time. *$P = 0.045$, **$P = 0.002$, $P = 0.001$ and $P = 0.005$ for the comparisons between d3 and d14, d5 and d14 and d7 and d14, respectively; two-tailed t-test. **e**, The relative viability of 5 near-euploid (CAL51, EN, MHHNB11, SW48 and VMCUB1) and 5 highly-aneuploid (MDAMB468, NCIH1693, PANC0813, SH10TC and A101D) cell lines to 72h and 14 days exposure to the SAC inhibitor reversine. *$P = 0.012$ and $P = 0.037$, for 3d and 14d time points, respectively; two-tailed Wilcoxon rank-sum test.
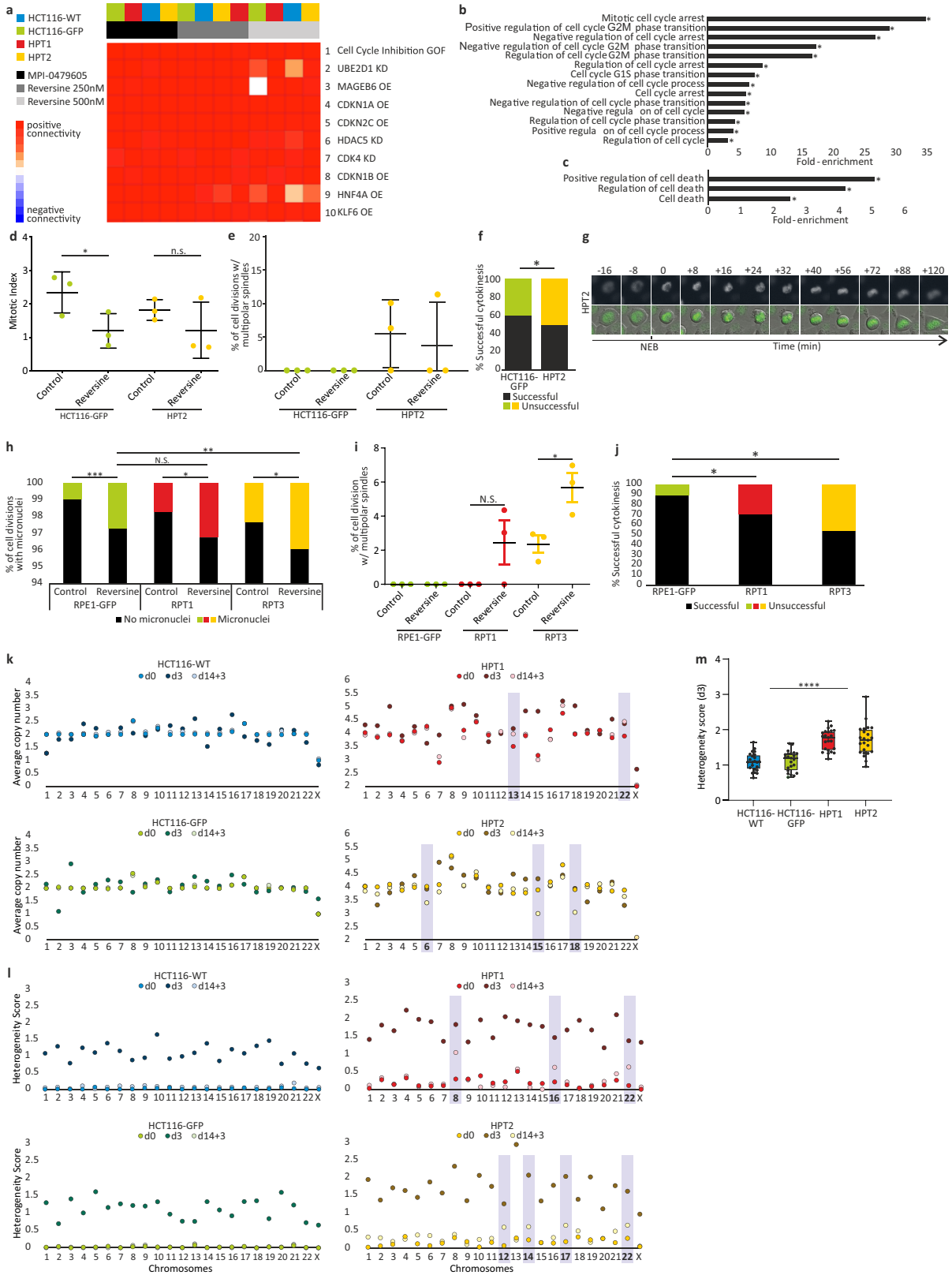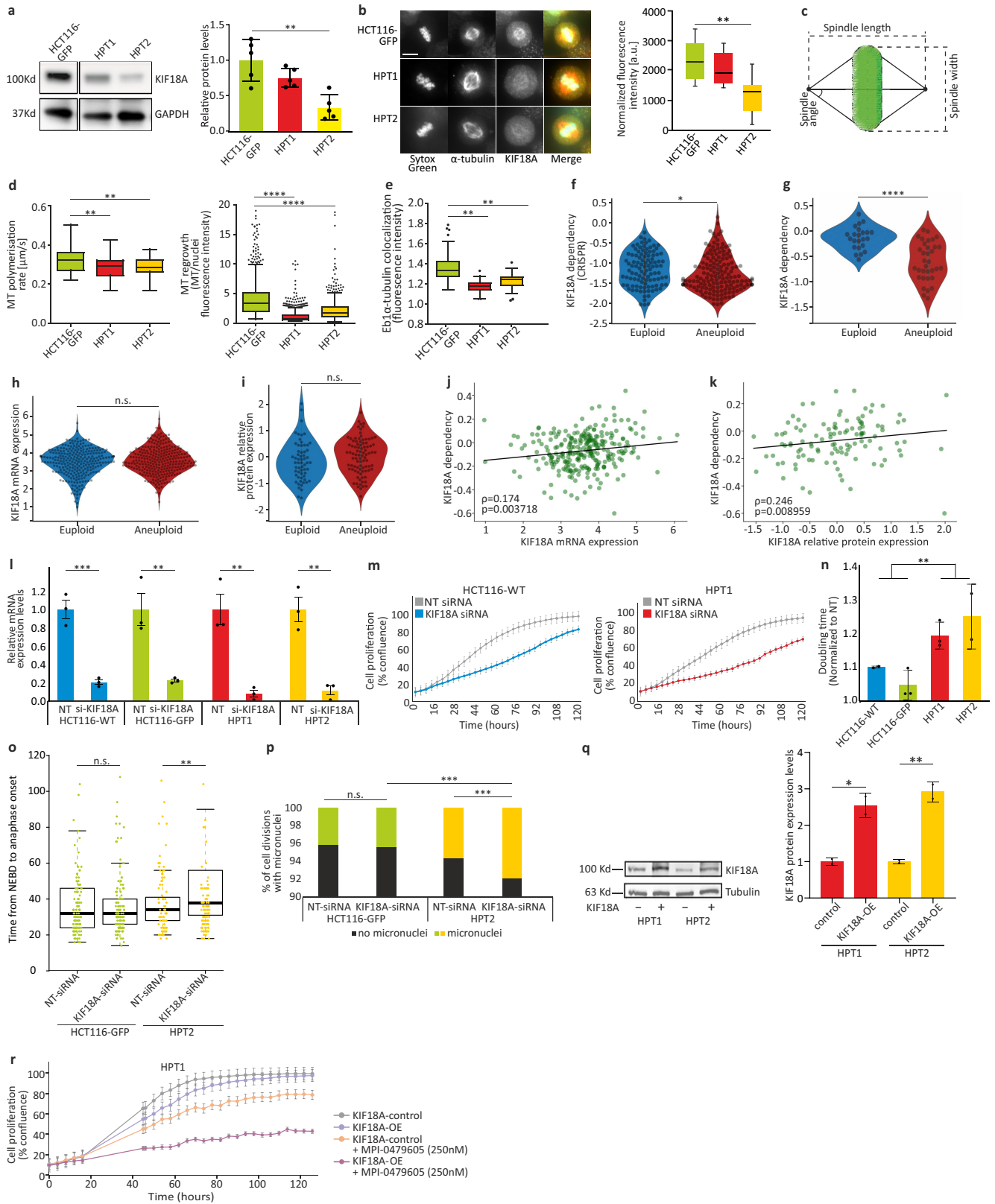
Extended Data Fig. 8 | See next page for caption.

Article

Extended Data Fig. 8 | Transcriptional, cellular and karyotypic characterization of SACi in aneuploid cells. a, The top 10 results of a Connectivity Map (CMap) query[63] of the transcriptional response of HCT116 and HPT cells to the SAC inhibitors, reversine (250nM and 500nM) and MPI-0479605 (250nM). The top connection is "Cell cycle inhibition", correctly identifying the expected mechanism of action of these compounds. GOF, gain of function; OE, overexpression; KD, knockdown. **b**, Functional enrichment of gene sets related to cell cycle regulation. Shown are the gene sets that were significantly more affected by SACi in the highly-aneuploid HPT1 and HPT2 cells than in the nearly-diploid HCT116-WT and HCT116-GFP cells. *$P < 0.05$, one-tailed Fisher's exact test. **c**, Functional enrichment of gene sets related to cell death. Shown are the gene sets that were significantly more affected by SACi in the highly-aneuploid HPT1 and HPT2 cells than in the nearly-diploid HCT116-WT and HCT116-GFP cells. *$P < 0.05$, one-tailed Fisher's exact test. **d**, The mitotic index of HCT116 and HPT cells cultured under standard conditions or exposed to the SAC inhibitor reversine (500nM) for 24h. *$P = 0.035$; n.s., $P = 0.17$; two-tailed t-test; Error bars, s.d.; $n = 3$ biological replicates. **e**, Imaging-based quantification of the prevalence of cell divisions with multipolar spindles in HCT116 and HPT cell lines cultured under standard conditions or treated with reversine (500nM) for 24hr; $n = 3$ biological replicates. Error bars, s.d. **f**, The prevalence of premature mitotic exit (cytokinesis failure) in HCT116 and HPT cells exposed to the SAC inhibitor reversine (500nM) for 24h. *$P = 0.047$; two-tailed Fisher's exact test. **g**, Representative images of premature mitotic exit in HPT2 cells exposed to reversine (500nM). $T = 0$ defines nuclear envelope breakdown (NEB). Scale bar, 10μm. **h**, The prevalence of micronuclei formation in RPE1 and RPT cells cultured under standard conditions or exposed to the SAC inhibitor reversine (500nM) for 24h. n.s., $P > 0.05$; *$P = 0.013$ and $P = 0.015$ for the differences between the treated and untreated RPT1 and RPT3 cells, respectively; **$P = 0.004$; ***$P < 0.0002$; two-tailed t-test. **i**, The prevalence of cell divisions with multipolar spindles in RPE1 and RPT cells cultured under standard conditions or exposed to the SAC inhibitor reversine (500nM) for 24h. n.s., $P > 0.05$; *$P = 0.028$; two-tailed t-test. Error bars, s.d. **j**, The prevalence of premature mitotic exit (cytokinesis failure) in RPE1 and RPT cells exposed to the SAC inhibitor reversine (500nM) for 24h. *$P = 0.044$ and $P = 0.019$ for the comparisons between RPE1 and RPT1 or RPT3, respectively; two-tailed t-test. **k**, Chromosomal copy number states of HCT116 and HPT cells at each of the 3 time points that were sequenced by scDNaseq. Differences between the pre-treated (d0) and post-treated (d14+3) populations are highlighted. **l**, Chromosomal heterogeneity scores of the HCT116 and HPT cells at each of the 3 time points. Highly-heterogeneous chromosomes in the post-treated populations (d14+3) are highlighted; $n = 23$ chromosomes. **m**, Comparison of the chromosomal heterogeneity scores between the near-diploid HCT116 cells and the highly-aneuploid HPT cells. Bar, median; box, 25th and 75th percentile; whiskers, 1.5 X IQR; circles, individual chromosomes. ****$P = 2e-09$; two-tailed t-test.
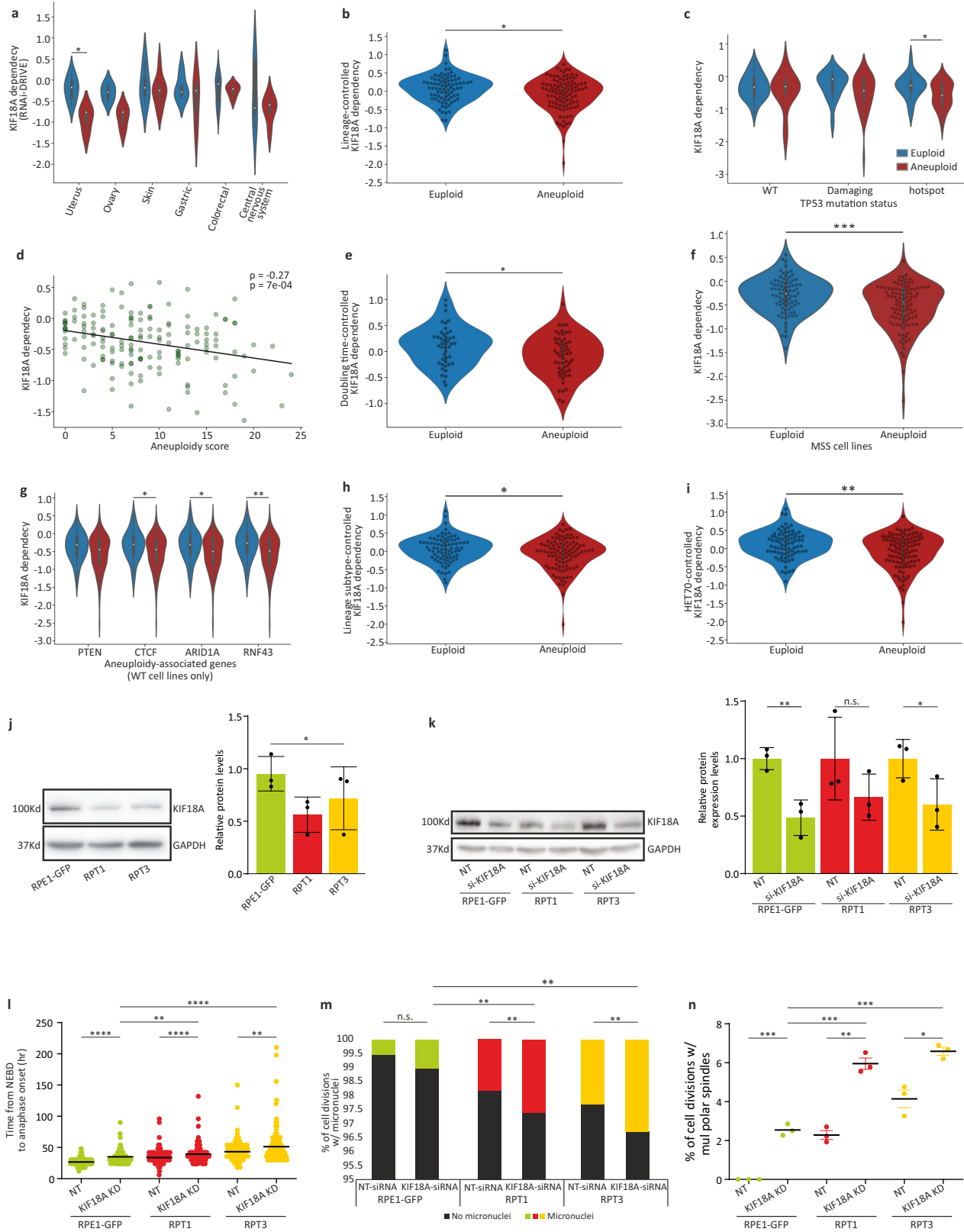
Extended Data Fig. 9 | See next page for caption.

Article

Extended Data Fig. 9 | Increased sensitivity of aneuploid cancer cells to perturbation of the mitotic kinesin KIF18A. a, Left: western blot of KIF18A protein expression levels in HCT116 and HPT cell lines. Right: Quantification of KIF18A expression levels (normalized to GAPDH). $**P = 0.002$; two-tailed t-test; $n = 5$ biological replicates. **b**, Left: Imaging kinetochore-bound KIF18A protein levels in HCT116-GFP, HPT1 and HPT2 cells, Scale bars, 10μm. Right: Immunofluorescence-based quantification of KIF18A protein levels. $**P < 0.01$, two-tailed t-test. Bar, median; box, 25th and 75th percentile; whiskers, 1.5 X IQR. **c**, Schematics of the definitions of spindle length, width and angle. **d**, Left: Imaging-based quantification of microtubule polymerization rate in HCT116 and HPT cells cultured under standard conditions. Right: Imaging-based quantification of microtubule regrowth following complete depolymerization in HCT116 and HPT cells. Bar, median; box, 25th and 75th percentile; whiskers, 1.5 X IQR; circles, individual cell lines. $*P < 0.05$; $**P < 0.01$; $****P < 1e-4$; two-tailed t-test. **e**, Imaging-based quantification of EB1α-tubulin co-localization in HCT116 and HPT cells cultured under standard conditions. $**P < 0.01$. Bar, median; box, 25th and 75th percentile; whiskers, 1.5 X IQR. **f**, The sensitivity of near-euploid and highly-aneuploid cancer cell lines to the knockout of *KIF18A* in the CRISPR-Achilles data set. The more negative a value, the more essential the gene is in that cell line. $*P = 0.034$; two-tailed t-test. **g**, The sensitivity of near-euploid and highly-aneuploid cancer cell lines to the knockdown of *KIF18A* in the DRIVE RNAi screen (top vs. bottom 10% of cell lines). The more negative a value, the more essential the gene is in that cell line. $****P = 3e-06$; two-tailed t-test. **h**, Comparison of the mRNA expression levels of *KIF18A* between near-euploid and highly-aneuploid cancer cell lines. n.s., $P > 0.05$; two-tailed t-test. **i**, Comparison of the protein expression levels of KIF18A between near-euploid and highly-aneuploid cancer cell lines. n.s., $P > 0.05$; two-tailed t-test. **j**, The correlation between *KIF18A* mRNA expression and the genetic dependency on this gene in the Achilles-RNAi screen. Spearman's $\rho = 0.17$ ($P = 0.004$). **k**, The correlation between KIF18A protein expression and the genetic dependency on this gene in the Achilles-RNAi screen. Spearman's $\rho = 0.25$ ($P = 0.009$). **l**, Relative mRNA expression levels of KIF18A, confirming successful siRNA-mediated KD in all cell lines 72h post-transfection. $**P = 0.006$, $P = 0.003$ and $P = 0.002$ for HCT116-GFP, HPT1 and HPT2, respectively; $***P = 0.0007$; one-tailed t-test. **m**, Proliferation curves of HCT116 and HPT1 cells cultured in the presence of a KIF18A-targeting siRNA, or a non-targeting control siRNA. **n**, Comparison of the doubling times of HCT116 and HPT cells following siRNA-mediated KIF18A knockdown. $**P = 0.001$; two-tailed t-test. **o**, Time-lapse imaging-based quantification of the time from nuclear envelope breakdown (NEBD) to anaphase onset in HCT116 and HPT cell lines exposed to non-targeting or KIF18A-targeting siRNAs for 72h. n.s, $P > 0.05$; $**P = 0.003$; two-tailed t-test. Bar, median; box, 25th and 75th percentile; whiskers, 1.5 X IQR; circles, individual cell lines. **p**, The prevalence of micronuclei formation in HCT116 and HPT cells exposed to non-targeting or KIF18A-targeting siRNAs for 72h. n.s., $P > 0.05$; $***P < 0.001$; two-tailed Fisher's exact test. **q**, Relative protein expression levels of KIF18A, confirming successful KIF18A overexpression in the highly-aneuploid HPT1 and HPT2 cell lines 48h post-transfection. Left: western blot of KIF18A protein expression levels in HPT1 and HPT2 before and after KIF18A overexpression. Right: quantification of KIF18A expression levels (normalized to α-Tubulin). $*P = 0.013$, $**P = 0.005$; one-tailed t-test; $n = 2$ biological replicates. In all bar plots and line plots, data represent the mean ± s.d. unless otherwise noted; $n = 3$ biological replicates unless otherwise noted. **r**, Proliferation curves of HPT1 cells before and after overexpression of *KIF18A* (KIF18A-OE), in the absence or presence of MPI-0479605 (250nM).

Extended Data Fig. 10 | See next page for caption.

Article

Extended Data Fig. 10 | Additional validation of the increased sensitivity of aneuploid cells to KIF18A inhibition. a, The sensitivity of near-euploid and highly-aneuploid cancer cell lines to the knockdown of KIF18A in the DRIVE RNAi screen across multiple cell lineages. *P = 0.022; two-tailed t-test. **b**, The sensitivity of near-euploid and highly-aneuploid cancer cell lines to the knockdown of KIF18A in the DRIVE RNAi screen, after accounting for lineage-specific differences in gene dependency scores using linear regression. *P = 0.012; two-tailed t-test. **c**, The sensitivity of near-euploid and highly-aneuploid cancer cell lines to the knockdown of KIF18A in the DRIVE RNAi screen, across *TP53* mutation classes. *P = 0.026; two-tailed t-test. **d**, The correlations between AS and the dependency on KIF18A in the DRIVE RNAi screen, for cell lines that have not undergone whole-genome duplication (that is, cell lines with basal ploidy of n = 2). Spearman's ρ = -0.27 (P = 7e-04). **e**, The sensitivity of near-euploid and highly-aneuploid cancer cell lines to the knockdown of KIF18A in the DRIVE RNAi screen, after removing the effect of doubling time on gene dependency scores using linear regression. *P = 0.022; two-tailed t-test. **f**, The sensitivity of near-euploid and highly-aneuploid cancer cell lines without microsatellite instability (MSS lines only) to the knockdown of KIF18A in the DRIVE RNAi screen. ***P = 3e-04; two-tailed t-test. **g**, The sensitivity of near-euploid and highly-aneuploid cancer cell lines to the knockdown of KIF18A in the DRIVE RNAi screen, in cell lines that are WT for the 4 genes most selectively mutated in aneuploid human tumours (after *TP53*)[12]. *P = 0.021 and P = 0.02, for CTCF and ARID1A, respectively; **P = 0.004; two-tailed t-test. **h**, The sensitivity of near-euploid and highly-aneuploid cancer cell lines to the knockdown of KIF18A in the DRIVE RNAi screen, after removing the effect of lineage subtype on gene dependency scores using linear regression. *P = 0.024; two-tailed t-test. **i**, The sensitivity of near-euploid and highly-aneuploid cancer cell lines to the knockdown of KIF18A in the DRIVE RNAi screen, after removing the effect of HET70 scores on gene dependency scores using linear regression. **P = 0.003; two-tailed t-test. **j**, Left: western blot of KIF18A protein expression levels in RPE1 and RPT cell lines. Right: Quantification of KIF18A expression levels (normalized to GAPDH). *P = 0.023; one-tailed t-test. Data represent the mean ± s.d.; n = 3 biological replicates. **k**, Relative protein expression levels of KIF18A, confirming successful KIF18A knockdown in the RPE1 and RPT cell lines 72h post-transfection. Left: western blot of KIF18A protein expression levels in RPE1, RPT1 and RPT3 before and after siRNA-mediated KIF18A knockdown. Right: Quantification of KIF18A expression levels (normalized to α-Tubulin). *P = 0.034, **P = 0.004; one-tailed t-test. Data represent the mean ± s.d.; n = 3 biological replicates. **l**, Time-lapse imaging-based quantification of the time from nuclear envelope breakdown (NEBD) to anaphase onset in RPE1 and RPT cell lines exposed to non-targeting or *KIF18A*-targeting siRNAs for 72h. **P < 0.01; ****P < 1e-04; two-tailed t-test. **m**, The prevalence of micronuclei formation in HCT116 and HPT cells exposed to non-targeting or *KIF18A*-targeting siRNAs for 72h. n.s., P > 0.05; **P < 0.01; ***P < 0.001; two-tailed Fisher's exact test. **n**, Imaging-based quantification of the prevalence of cell divisions with multipolar spindles in RPE1 and RPT cell lines treated with non-targeting control or KIF18A-targeting siRNAs for 72h. *P < 0.05; **P < 0.01; ***P < 0.001; two-tailed t-test; Error bars, s.d.; n = 3 biological replicates.

nature research

Corresponding author(s):   Uri Ben-David

Last updated by author(s):   Nov 9, 2020

Reporting Summary

Nature Research wishes to improve the reproducibility of the work that we publish. This form provides structure for consistency and transparency in reporting. For further information on Nature Research policies, see Authors & Referees and the Editorial Policy Checklist.

Statistics

For all statistical analyses, confirm that the following items are present in the figure legend, table legend, main text, or Methods section.

n/a	Confirmed	
☐	☒	The exact sample size (n) for each experimental group/condition, given as a discrete number and unit of measurement
☐	☒	A statement on whether measurements were taken from distinct samples or whether the same sample was measured repeatedly
☐	☒	The statistical test(s) used AND whether they are one- or two-sided *Only common tests should be described solely by name; describe more complex techniques in the Methods section.*
☐	☒	A description of all covariates tested
☐	☒	A description of any assumptions or corrections, such as tests of normality and adjustment for multiple comparisons
☐	☒	A full description of the statistical parameters including central tendency (e.g. means) or other basic estimates (e.g. regression coefficient) AND variation (e.g. standard deviation) or associated estimates of uncertainty (e.g. confidence intervals)
☐	☒	For null hypothesis testing, the test statistic (e.g. F, t, r) with confidence intervals, effect sizes, degrees of freedom and P value noted *Give P values as exact values whenever suitable.*
☒	☐	For Bayesian analysis, information on the choice of priors and Markov chain Monte Carlo settings
☒	☐	For hierarchical and complex designs, identification of the appropriate level for tests and full reporting of outcomes
☐	☒	Estimates of effect sizes (e.g. Cohen's d, Pearson's r), indicating how they were calculated

Our web collection on statistics for biologists contains articles on many of the points above.

Software and code

Policy information about availability of computer code

Data collection

All software used in data collection were published , and are described in the Methods section of the paper. No commercial SW were used.
Low-pass whole-genome sequencing alignment was performed using the BWQ (0.7.12) backtrack algorithm. Single cell sequencing alignment was performed using Bowtie2 (v2.2.4, duplicate reads marked with BamUtil (v1.0.3).

Data analysis

All SW used for data analysis are commercially or publicly available, and are described in the Methods section:
Genomic data sets were downloaded from the Dependancy Map portal (www.depmap.org/portal/).
Experimantal confounders in gene expression data were corrected using ComBat (v3).
Functional annotation enrichment analysis was performed using DAVID v6.8 and GSEA v4.0.0.
Microscopy-based analysis of cell proliferation was performed using IncuCyte S3 Live Cell Analysis System (Essen Bioscience).
Cell masking in representative images was performed using Ilastik image analysis SW. Fluorescence signal quantification was performed using the SlideBook SW.
Copy number data were detected using the HMMCopy algorithm. Aneuploidy analysis of scDNAseq data was performed using AneuFinder (v1.14.0).
Flow cytometry data were analyzed using the Kaluza Analysis SW.
Statistical analysis and plotting were done in GraphPad Prism v8.4.3 or in Office 2016 Excel.
The following packages were used: scikit-learn 'RandomForestRegressor', R packages: 'stats', 'drc', 'limma-trend', 'hclust', 'fgsea'.

For manuscripts utilizing custom algorithms or software that are central to the research but not yet described in published literature, software must be made available to editors/reviewers. We strongly encourage code deposition in a community repository (e.g. GitHub). See the Nature Research guidelines for submitting code & software for further information.

Data

Policy information about availability of data

All manuscripts must include a data availability statement. This statement should provide the following information, where applicable:
- Accession codes, unique identifiers, or web links for publicly available datasets
- A list of figures that have associated raw data
- A description of any restrictions on data availability

All datasets are available within the article, its Supplementary Information, or from the corresponding authors upon request. Cell line aneuploidy profiles and scores are available at the DepMap portal (www.depmap.org/portal/). The analyzed CCLE genomic data is available in https://doi.org/10.6084/m9.figshare.11384241.v2. LP-WGS data have been deposited to SRA with BioProject accession number PRJNA672256.

Field-specific reporting

Please select the one below that is the best fit for your research. If you are not sure, read the appropriate sections before making your selection.

☒ Life sciences   ☐ Behavioural & social sciences   ☐ Ecological, evolutionary & environmental sciences

For a reference copy of the document with all sections, see nature.com/documents/nr-reporting-summary-flat.pdf

Life sciences study design

All studies must disclose on these points even when the disclosure is negative.

Sample size	All available human cancer cell lines were used for the comparisons of the Achilles-shRNA, DRIVE-shRNA, Achilles-CRISPR, GDSC and CTD2 data sets. For validation experiments, we selected 5 highly-aneuploid and 5 near-diploid cell lines for practical reasons. For isogenic cell line systems (HCT/HPT, RPE1/RPT, RPE1/aneuploid clones), all existing clones were used.
Data exclusions	No data were excluded from the analyses.
Replication	All experiments were performed at least 3 times. The experimental findings were reliably reproduced, and all attempts were included in the presentation unless technical failures prevented the completion of the experiment.
Randomization	No randomization was done, as all available cell lines were used (therefore, randomization was not required).
Blinding	Genetic and transcriptional profiling were performed without the investigators' knowledge of each sample identity. Investigators were not blind to sample identity during the in vitro experiments because cell lines required different culture conditions.

Reporting for specific materials, systems and methods

We require information from authors about some types of materials, experimental systems and methods used in many studies. Here, indicate whether each material, system or method listed is relevant to your study. If you are not sure if a list item applies to your research, read the appropriate section before selecting a response.

Materials & experimental systems

n/a	Involved in the study
☐	☒ Antibodies
☐	☒ Eukaryotic cell lines
☒	☐ Palaeontology
☒	☐ Animals and other organisms
☒	☐ Human research participants
☒	☐ Clinical data

Methods

n/a	Involved in the study
☒	☐ ChIP-seq
☐	☒ Flow cytometry
☒	☐ MRI-based neuroimaging

Antibodies

Antibodies used	The following primary antibodies were used: anti-Kif18A rabbit (1:500), affinity-purified polyclonal antibody raised against an N-terminal GST-tagged fragment (Kif18AbN), a gift from Dr. Thomas Mayer, University of Konstanz, Germany; anti-Kif18A rabbit (1:5,000), Bethyl Laboratories (catalog no. A301-080A); anti-GAPDH goat (1:1,000), Abcam (catalog no. ab9483); anti-α-Tubulin mouse (1:2,000), Sigma (catalog no. T6199).
Validation	Antibodies were selected based on their use in the literature in human cancer cell lines, and previous experience of the investigators. Full antibody information is provided in the Methods section of the paper. Positive and negative controls were used in all experiments including antibodies.

Eukaryotic cell lines

Policy information about cell lines

Cell line source(s)	Established commonly-used human cancer cell lines were used in this study: MDAMB468, A101D, EN, VMCUB1, CAL51, SW48, SH10TC, NCIH1693, MHHNB11 and PANC0813 were purchased from the Cancer Cell Line Encyclopedia. The HCT116/HPT and RPE1/RPT lines were genetically manipulated by the Storchova lab, and the RPE1 line was also manipulated by the Santaguida lab.
Authentication	Cell line authentication was performed using SNP-based DNA fingerprinting or through copy number profiling of the cell lines.
Mycoplasma contamination	All cell lines tested negative to mycoplasma contamination using a Lonza kit.
Commonly misidentified lines (See ICLAC register)	Cell lines are not in the list of misidentified cell lines.

Flow Cytometry

Plots

Confirm that:

☒ The axis labels state the marker and fluorochrome used (e.g. CD4-FITC).

☒ The axis scales are clearly visible. Include numbers along axes only for bottom left plot of group (a 'group' is an analysis of identical markers).

☒ All plots are contour plots with outliers or pseudocolor plots.

☒ A numerical value for number of cells or percentage (with statistics) is provided.

Methodology

Sample preparation	For cell cycle and cell death analyses, cells were trypsinized and incubated in cold PBS supplemented with 5% fetal calf serum (Sigma-Aldrich; PBS-FACS). DNA was stained either by propidium iodide (PI) or by Hoechst. For PI staining, cells were fixed in cold 70% ethanol, added dropwise while vortexing, and incubated on ice for 30 minutes. Cells were centrifuged and pellets were washed twice with PBS-FACS. 50 µl RNase A solution (100 µg/ml in PBS) was added to the pellet, followed by staining with 400 µl PI solution (50 µg/ml in PBS) per million cells. Cells were incubated for 10' at 25oC. For Hoechst staining, pellets were incubated in the dark with 10 mg/ml Hoechst 33358 for 15' at 4oC.
Instrument	Data acquisition was performed using the CytoFLEX flow cytometer (Beckman Coulter) or the BD FacsJAZZ cell sorter (BD Biosciences).
Software	Data analysis was performed using the Kaluza Analysis software 2.1 (Beckman Coulter).
Cell population abundance	No sorting was performed.
Gating strategy	An SSC-A/FSC-A gate was set in order to exclude cell debris, and an FSC-A/FSC-H gate was then set in order to exclude doublets. Cell cycle phases were determined manually using linear gating based on the 2N and 4N peaks of the histogram. Cell death was assessed by quantifying the fraction of cells in the subG1 population, and mitotic arrest was assessed by quantifying the fraction of cells in the G2/M population.

☒ Tick this box to confirm that a figure exemplifying the gating strategy is provided in the Supplementary Information.